Coseismic Fault Slip and Transtensional Stress Field in the Hovsgol Basin Revealed by the 2021 Mw 6.7 Turt, Mongolia Earthquake

Xiaoge Liu[1], Wenbin Xu[1], Natalia Radziminovich[2], Nan Fang[1], and Lei Xie[3]

[1]Central South University
[2]Institute of the Earth‘s crust, Siberian Branch of the Russian Academy of Sciences
[3]The Hong Kong Polytechnic University

November 26, 2022

Abstract

Knowledge of the regional crustal deformation and stress field is fundamental to understanding and constrain the ongoing Hovsgol basin evolution. The 2021 Mw 6.7 Turt earthquake provides an unprecedented opportunity to probe the local tectonic stress field and upper crust deformation. We investigate the coseismic surface displacements and invert fault slip models using Interferometric Synthetic Aperture Radar observations and teleseismic data. The mainshock occurred as a result of normal faulting with a right-lateral strike-slip component on an NW striking plane, which is consistent with the transtensive local stress field inverted from regional focal mechanisms. Our results also suggest that the current deformation of the Hovsgol basin is dominated by half-graben forming. The 1950 Mondy earthquake may advance the 2021 Turt earthquake by ˜7% recurrence interval, meanwhile, the 2021 Turt earthquake may increase the potential seismic hazard on the neighbor Mondy and South Hovsgol Fault, which deserves more attention.

Coseismic Fault Slip and Transtensional Stress Field in the Hovsgol Basin Revealed by the 2021 Mw 6.7 Turt, Mongolia Earthquake

Xiaoge Liu[1], Wenbin Xu[1,*], Natalia A. Radziminovich[2], Nan Fang[1], Lei Xie[3]

[1]School of Geosciences and Info-Physics, Central South University, Changsha 410083, Hunan, P.R. China

[2]Institute of the Earth's Crust, Siberian Branch of the Russian Academy of Sciences, Lermontov Str., 128, Irkutsk 664033, Russia

[3]The Department of Land Surveying and Geo-Informatics, The Hong Kong Polytechnic University, Hong Kong, China

*Corresponding author: Wenbin Xu (wenbin.xu@csu.edu.cn)

Key points:

- Transtensional coseismic slip and stress field in Hovsgol basin are revealed with InSAR, teleseismic data and focal mechanisms.
- Current deformation of Hovsgol basin is dominated by half-graben forming.
- The 1950 Mondy earthquake may advance the 2021 Turt earthquake increasing potential seismic hazard on the Mondy and South Hovsgol Fault.

Abstract

Knowledge of the regional crustal deformation and stress field is fundamental to understanding and constrain the ongoing Hovsgol basin evolution. The 2021 Mw 6.7 Turt earthquake provides an unprecedented opportunity to probe the local tectonic stress field and upper crust deformation. We investigate the coseismic surface displacements and invert fault slip models using Interferometric Synthetic Aperture Radar observations and teleseismic data. The mainshock occurred as a result of normal faulting with a right-lateral strike-slip component on an NW striking plane, which is consistent with the transtensive local stress field inverted from regional focal mechanisms. Our results also suggest that the current deformation of the Hovsgol basin is dominated by half-graben forming. The 1950 Mondy earthquake may advance the 2021 Turt earthquake by ~7% recurrence interval, meanwhile, the 2021 Turt earthquake may increase the potential seismic hazard on the neighbor Mondy and South Hovsgol Fault, which deserves more attention.

Plain Language Summary

The 2021 Mw 6.7 Turt earthquake has been the strongest earthquake recorded instrumentally for the Hovsgol basin. We used InSAR and teleseismic data to constrain seismogenic fault geometry. InSAR data show the subsidence up to 0.2 m. The comparable normal and strike slip components are found after slip distribution inversions. The maximum coseismic slip was 1.2 m at a depth of 7 km. We also invert the stress fields using the regional focal mechanisms. We found that the 2021 Turt earthquake occurred in the transtensional stress regime, which is consistent with the observed transtensional coseismic slip. Our results also suggest that the current deformation of Hovsgol basin is dominated by half-graben forming. Considering that the earthquake occurred in the junction zone of two large faults, namely the North Hovsgol fault and Mondy fault, an Mw6.9 earthquake occurred on the latter 70 years ago. Based on the Coulomb stress change calculation, we found that the 1950 Mondy earthquake may advance the 2021 Turt earthquake by ~7% recurrence interval, meanwhile potential seismic hazard on the neighbor Mondy and South Hovsgol Fault deserves more attention.

Key words: Coseismic InSAR displacement, Fault geometry and slip distribution, Transtensional stress field, Stress heterogeneity, Half-graben, Coulomb stress change

1. Introduction

The Hovsgol basin is situated in the western closure of the Baikal rift system. This rift system is located within the Asian continent interior, and is one of the most active discrete rifts representing the early stages of continental split-up (Petit and Déverchère, 2006). GPS measurements suggest that ~15% of the India-Eurasia convergence (~40 mm/yr) is accommodated within the Baikal Rift System and Mongolia (Calais et al., 2003; Wang and Shen, 2020). The western part of the Baikal rift system is located within the Central Asian mobile belt which traces along the southern margin of the Siberian craton. This belt near the Siberian craton consists of a number of Precambrian and Early Paleozoic terranes (Gladkochub and Donskaya, 2009). The Cenozoic Hovsgol basin has been formed along the border of the Tuva-Mongolian Riphean microcontinent with the early Paleozoic Khamardaban block (Vasiliev et al., 1997). The basin is a half-graben with the steep western side bordered by the Hovsgol master fault. This graben-forming stage is still continuing, which divides the Hovsgol Unit into west-Hovsgol dome-blocky uplift and the east-Hovsgol arch-like structure during the neotectonics stage (Gladkochub and Donskaya, 2009).

The considered area is a key region where compression due to the Indo-Eurasia collision meets extension due to Baikal rifting. In the northern Mongolia, three narrow basins, oriented S-N, namely the Busingol, the Darkhad, and the Hovsgol basins, are supposed to be rift basins; however, the recent stress field here has been evaluated as transpression (Sankov et al., 2011). Reconstructed on tectonic fracturing, slickenside in outcrops of dated Cenozoic formations and basement rocks, the stress field of the Hovsgol basin shows temporal changes from extension in NW-SE direction in Miocene to compression in this direction for a short time in Late Pliocene, and then at the latest stage (Quaternary) to strike-slip and transpression stress field with orientations of NE-SW compression axis and NW-SE tension axis (Sankov et al., 2004). Thus, the present-day stress field in the region is defined as compressional stress regime (Ritz et al., 2000). However, there is no consensus on the type of stress regime in Hovsgol basin. Combined seismological focal mechanisms and geological observations, Delouis et al. (Delouis et al., 2002) provide the stress inversion results indicating the Hovsgol basin is under pure extensive stress regime, while wrench-extensional regime is also proposed for the Hovsgol basin (Petit et al., 1996; Radziminovich et al., 2016). In addition, the seismic

focal mechanism solutions of the 2021 Hovsgol mainshock from several organizations showed a consistent normal faulting (Fig. 1b). However, their magnitude of strike slip component and focal depth (10-20 km) is inconsistent (Table 1). These discrepancies indicate that the regional tectonic stress is rather complicated.

On 11 January 2021, an Mw 6.7 earthquake occurred in the northern part of the Hovsgol basin. It is the largest instrumentally recorded event here, providing an opportunity for studying the stress heterogeneity in the region. However, only a few geodetic studies were carried out with limited campaign GPS sites (Bayasgalan et al., 2005; Calais et al., 2003; Vergnolle et al., 2003), which are not located in the coseismic region. Fortunately, space geodetic Interferometric Synthetic Aperture Radar (InSAR) technology captures the coseismic surface displacement caused by the 2021 Turt earthquake. This permits us to study the crust deformation and stress regime in the Hovsgol basin. Here, we use Sentinel-1 Synthetic Aperture Radar (SAR) images to map the coseismic InSAR displacements following the 2021 Turt Mw 6.7 earthquake. Combining the teleseismic P-wave data, we jointly constrain the seismogenic fault geometry and finite slip model. Using the previous data on earthquake focal mechanisms, we make stress inversion to reveal how the displacement of the Turt earthquake relates to the stress field. Finally, we analyze seismic risk in the Hovsgol region by estimating

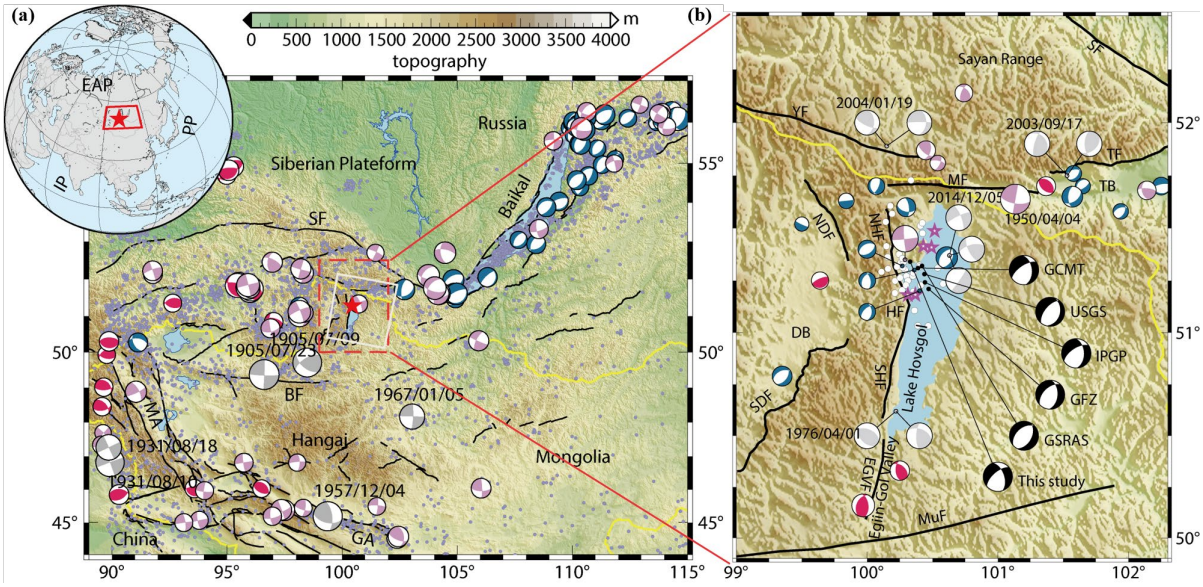

the Coulomb stress change after the Turt earthquake.

Fig. 1. Regional seismotectonic context around the 2021 Turt, Mongolia earthquake. (a) Red star represents the epicenter of the main shock from USGS. Blue, pink, and red focal mechanisms represent normal-,

strike-slip, and thrust-dominated events from International Seismological Centre (ISC, http://www.isc.ac.uk/iscbulletin/search/fmechanisms/interactive/), respectively. Gray moment tensors are historical great earthquakes with M>7. Purple dots are epicenters for earthquakes since 1900. Black lines are the main active faults from GEM Global Active Faults (https://github.com/GEMScienceTools/gem-global-active-faults). White rectangles represent the spatial extent of Sentinel-1 SAR data from one descending track (DT4). Yellow line shows the border between China, Mongolia and Russia. Dashed red rectangle bounds the extent of enlarged Fig. 1b. The inset shows the location of the study area. IP, Indian Plate; PP, Pacific Plate; EAP, Eurasian Plate. (b) The detailed tectonic background in the study area. Black focal mechanisms represent solutions for the mainshockfrom different catalogs (Table 1). White dots are the aftershocks from USGS, and six Mw > 5 were highlighted by purple starts. SF, Sayan Fault; BF, Bolnay Fault; TF, Tunka Fault; MF, Mondy Fault; YF, Yamaatinskiy Fault; HF, Hovsgol Fault including North HF (NHF) and South HF (SHF); NDF, North Darkhat Fault; SDF, South Darkhat Fault; EGVF, Egiin-Gol Valley Fault; MuF, Murn Fault; MA, Mongolian Altay; GA, Gobi Altay; TB, Tunka Basin; DB, Darkhat Basin. Note that the SHF and MuF are compiled from previous studies and geomorphology (Jolivet et al., 2013; Petit et al., 2002; Ritz et al., 2018; Schlupp and Cisternas, 2007).

2. Data Processing and Inversion Methods

2.1. Coseismic Data Processing

2.1.1. InSAR Data

The Turt earthquake occurred in the remote northwestern of Mongolia, where few in-situ geodetic observations (i.e., GPS) are available near the epicenter (Calais et al., 2003; Wang and Shen, 2020). However, the good condition of arid climate and low erosion rates (Meltzer et al., 2019) permit us to employ InSAR technology to obtain the space geodetic displacements for this earthquake even with the C-band SAR images. SAR data acquired by the Sentinel-1 satellite provide a unique opportunity to quantify surface displacements of the Turt earthquake and to constrain the activated normal fault structures beneath the Lake Hovsgol (Fig. 1). Using the Gamma software (Wegmuller et al., 2015), high-accuracy coregistration of the primary and secondary Single Look Complex (SLC) products from descending tracks were firstly carried out (Table S2). Then, we constructed coseismic interferograms with the coregistrated primary and secondary SLCs. After removing the effect of topography with the 30 m Shuttle Radar Topography Mission digital elevation model (Farr et al., 2007), an improved

power spectrum filter method was applied to minimize the phase noise in the interferograms (Li et al., 2008). We unwrapped the filtered pairs of interferograms by a minimum cost flow method (Chen and Zebker, 2001), and geocoded the unwrapped interferograms to obtain the coseismic surface displacement fields. Considering the substantial topographic relief surrounding the Lake Hovsgol, possible topography-dependent tropospheric delay was estimated and removed (Xu et al., 2017).

2.1.2. Teleseismic Data

In addition to InSAR data, we also collected P wave records from 43 teleseismic stations at epicentral distances between 30° and 90° (Fig. S1) compiled by the Incorporated Research Institutions for Seismology (IRIS). The initial P wave records were firstly processed to minimize the influence of instrument response (Wald et al., 1996), and then a band-pass filter (0.01-0.5 Hz) was applied to suppress the noises. In addition, the teleseismic stations in the southern azimuth were excluded due to the low signal-to-noise ratio. Time window of waveforms was tapered as 98 s with 30 s before the initial arrivals (Figs. 2 and S2). The global velocity model AK135 is used for teleseismic Green's function calculation.

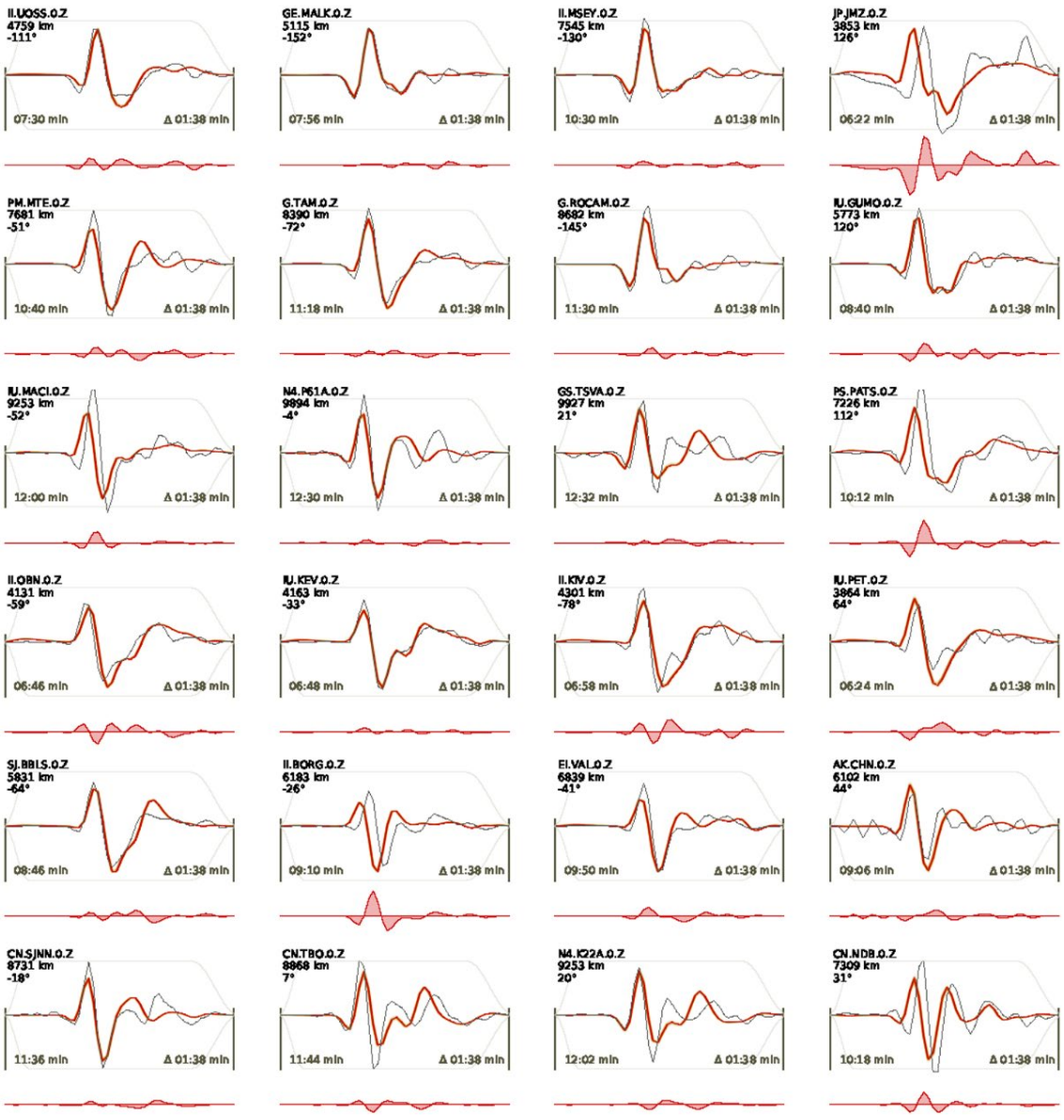

Fig. 2. Comparison between the observed teleseismic P waves and the synthetic waveforms obtained from the joint inversion of uniform fault slip model. The filtered (0.01–0.1 Hz) displacement waveform data (gray line) and the filtered synthetic displacement waveforms (red line) are shown together. Brown shading indicates 100 random draws of the filtered synthetic waveform displacements from the posterior probability density. Red-line polygons below each waveform submap represent the residual waveforms. Each sub-panel is annotated with the station name, component, the distance, and azimuth angle from the maximum a-posterior solution from the center of the reference fault. The arrival time and the duration of each station are shown in the lower left and right, respectively.

2.2. Fault Geometry and Distributed Slip Inversion

Before making an inversion of the Turt earthquake seismogenic fault geometry, we first downsampled the InSAR interferograms with a quadtree algorithm (Jónsson et al., 2002) to a computationally tractable size. Covariances of the downsampled data are estimated with the variability of raw observations within the downsampled grids and employed to weight the observations in the following inversions. In order to provide extra constrain on the fault geometry, P wave records data from IRIS and GEOFON are also introduced. The variances of P-wave data are estimated based on the data fluctuation before the P-wave arrival time. Bayesian Earthquake Analysis Tool (BEAT) is applied to determine the fault geometry parameters and their uncertainties (Vasyura-Bathke et al., 2020). To broadly cover the solution space and better quantify the associated uncertainties, a relatively loose sampling boundary is set up for fault geometry parameters according to prior knowledge (e.g., focal mechanisms from USGS/GCMT/GFZ/IPGP/GSRAS etc.) (Table 1 and Table S3). More detailed information about the nonlinear inversion can be found in (Vasyura-Bathke et al., 2020).

To resolve a distributed slip coseismic model fitting the observations better, we fixed the fault geometry derived from joint InSAR and teleseismic data inversion and extended the fault size with length of 50 km and width of 30 km (24 km in depth), and the fault was divided into 2×2 km subfaults. Being more finely discretized, sources are generally overparameterized, which commonly requires smoothness constraints to stabilize the solutions (Jónsson et al., 2002; Xu, 2017). We used the Laplacian regularization with smoothing factor determined from Cholesky decomposition of off-diagonal terms in a Gaussian prior $p(\mathbf{s}|\alpha)$. The maximum-a-posterior solution for strike, dip, and slip and the Laplacian smoothing factor α is obtained with sequential Monte Carlo method (Del Moral et al., 2006). More detailed information can be found in (Vasyura-Bathke et al., 2020).

2.3. Focal mechanism data and stress inversion

To make stress field inversion, we compiled a database of focal mechanism solutions for the Hovsgol region which come mainly from regional solutions published in the regular catalogs and some papers. The dataset includes focal solutions for 27 earthquakes that occurred before the 2021 Turt event (Table S1, Fig. 6). The vast majority of mechanisms were determined by the method of first motion polarity of P waves at the regional stations. Four

188 earthquakes have several solutions obtained by different authors. The strongest earthquake in
189 the area is the 1950 Mw6.9 Mondy earthquake occurred at the western termination of the
190 Tunka basins. Its fault-plane solution discussed in detail in (Delouis et al., 2002) was a sinistral
191 strike-slip movement on the western sublatitudinal segment of the Mondy fault. Other faults
192 in the western Tunka area have a reverse fault component that led to the conclusion about the
193 strike-slip or transpressive stress field here (Delouis et al., 2002; Radziminovich et al., 2016;
194 Sankov et al., 2004). However, the northern part of the Hovsgol basin is characterized mainly
195 by normal faulting in earthquake foci (Fig.1b, 5), though the 2014 Mw4.9 earthquake, which
196 occurred closer to the eastern side of the northern Hovsgol, had a different mechanism. Three
197 solutions are available for it (Table S1): the GCMT solution is a strike-slip with a normal fault
198 component, the first-motion solution is pure dip-slip with a flat and a steep planes of the NE
199 orientation (Dobrynina et al., 2018), and strike-slip solution with a reverse component is based
200 on the surface waves inversion (Melnikova et al., 2020). In contrast to the northern part of the
201 Hovsgol basin, its southern part is distinguished by reverse faulting (Figs. 1 and 5).

202 There are several methods for determining tectonic stress from focal mechanisms. The
203 most commonly used methods have been developed by (Gephart and Forsyth, 1984; Michael,
204 1984; Michael, 1987), which have been expanded and modified by (Lund and Slunga, 1999;
205 Martínez-Garzón et al., 2016; Vavryčuk, 2014). An iterative joint inversion method (Vavryčuk, 2014)
206 was adopted to calculate triaxial stress field σ_1, σ_2, σ_3 with $\sigma_1 > \sigma_2 > \sigma_3$ under the positive
207 compression stress convention, and the stress shape ratio $R = (\sigma_1 - \sigma_2)/(\sigma_1 - \sigma_3), 0 \le R \le 1$
208 describing the relative magnitudes of the principal compressive stresses (Warren-Smith et al.,
209 2019). This method is suitable for regions without information about actual tectonic faults.
210 This is attributed to a fault instability algorithm identifying a more likely nodal plane (Lund
211 and Slunga, 1999; Vavryčuk et al., 2013), which has little influence on the accuracy of stress field
212 orientations but significant improvement on the stress shape ratio. Additionally, this method
213 allows one to quantify the confidence intervals of optimal stress tensor by bootstrap
214 resampling approach (Michael, 1987), in which each nodal plane can be selected with equal
215 probability during the sampling.

216 For stress inversion, we used the focal mechanisms of earthquakes which occurred
217 before the Turt earthquake (Table S1, Fig.5) and the main shock (our solution) (Table 1 and
218 Table S1). Two samples were taken: the total sample given in Tables and only for the northern

219 part of the Hovsgol area. We estimated 2000 bootstrap samples with random noise 10° to
220 obtain 95% confidence region of optimal stress tensor. The average misfit angle α between
221 the observed and predicted fault slip directions can be used to evaluate the success of stress
222 inversion.
223

224 # 3. Results

225 ## 3.1. Coseismic InSAR displacement of the 2021 Turt earthquake

226 The excellent coherence and generally low noise level in the coseismic interferogram
227 characterize well-defined surface displacements associated with the Turt earthquake (Fig. 3).
228 The displacements are mainly distributed between the North Hovsgol Fault (NHF, Fig. 3) and
229 west bank of Lake Hovsgol. Few coseismic displacement can be observed on the neighboring
230 NNE-SSW striking South Hovsgol Fault (SHF), which may inhibit propagation of coseismic
231 rupture (Wilson et al., 2009). The descending coseismic displacement field shows obvious up to
232 ~20 cm surface subsidence away from the satellite line of sight (LOS) direction, indicating the
233 significant displacement zone is located at the hanging wall of the normal fault. There is no
234 obvious range decrease in the radar LOS direction except for the about ~5 cm LOS uplift
235 along the east bank of Lake Hovsgol (Fig. 3a). Interestingly, there exists a secondary fault
236 (NDF) on the west side of the seismogenic fault (~25 km), which may constrain the surface
237 displacement patterns on the footwall side of NHF (Fig. 3). It is worthy to note that coseismic
238 interferogram covers six Mw 5 and other aftershocks, which occurred on the same day of the
239 mainshock. In addition, the descending coseismic displacement contains more than one day of
240 other postseismic transients. These indicate that the coseismic displacements may be affected,
241 to some extent, by postseismic activities (Liu and Xu, 2019).
242

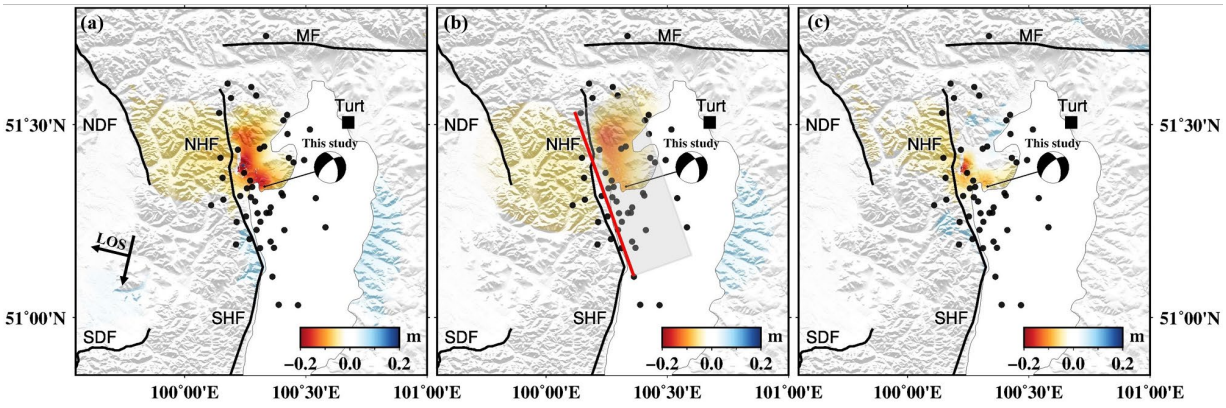

243

Fig. 3. Observed and modeled coseismic ground displacements in satellite line of sight (LOS) direction. (a) the observed ground deformation fields; (b) model predictions; (c) residuals between observations and models. Black moment tensor and dots represent USGS solution and aftershocks. The shade box in (b) represents the ground projection of the seismogenic fault with the red solid line indicating the fault trace. The fault abbreviations are identical to those in Fig. 1.

3.2. Fault Geometry and Slip Distribution

There are several fault-plane solutions for the Turt earthquake issued by different seismological agencies (Table 1). After the complete solution search for strike [0°, 360°], dip [0°, 90°], and rake [-180°, 180°] angles (Table S3), our results of nonlinear inversion show that the optimal fault plane was the NNW-SSE oriented plane (Table 1, Table S3). This confirms that the NHF is the seismogenic fault nucleating the 2021 Turt earthquake. The maximum posterior probability uniform slip model solution obtained after 10^6 iterations with sequential Monte Carlo method, raising the preferred fault plane of 35 km long and 14 km wide with a strike angle of 341°, a dip angle of 54°, and a rake angle of -146° (Table 1). This is consistent with the field-mapped fault trace along the west side of Lake Hovsgol (Fig. 1) and explains well the observed P waveform data (Fig. 2). Trade-offs between the fault parameters are not obvious (i.e., strike, dip and rake angles) as shown in the histograms of posterior probability distributions (Fig. 4).

Table 1. Source parameters for the 2021 Turt earthquake. USGS, U.S. Geological Survey (https://earthquake.usgs.gov); GCMT, Global Centroid-Moment Tensor Project (https://www.globalcmt.org/); GFZ, GeoForschungsZentrum (GEOFON) Moment Tensor Solutions (http://geofon.gfz-potsdam.de/eqinfo/); IPGP, Institute de Physique du Globe de Paris (http://www.ipgp.fr/fr); GSRAS, Geophysical Survey of Russian Academy of Sciences (http://www.ceme.gsras.ru/new/ssd_news.htm).

Source	Lon (°)	Lat (°)	Depth (km)	Strike (°)	Dip (°)	Rake (°)	*Mw*
USGS	100.438	51.281	11.5	16/219	32/60	-110/-78	6.74
GCMT	100.39	51.31	14.3	354/236	45/65	-143/-52	6.8
GFZ	100.47	51.21	18	4/226	47/51	-121/-60	6.7

IPGP	100.443	51.241	13	358/237	46/62	-139/-52	6.84
GSRAS	100.42	51.32	20	29/228	46/46	-103/0	Mb 6.5
This study	$100.33^{+0.01}_{-0.01}$	$51.34^{+0.01}_{-0.02}$	$8.9^{+0.6}_{-0.2}$	$340.4^{+1.0}_{-1.6}$	$53.9^{+7.0}_{-4.0}$	$-146.4^{+4.6}_{-5.8}$	$6.75^{+0.13}_{-0.17}$

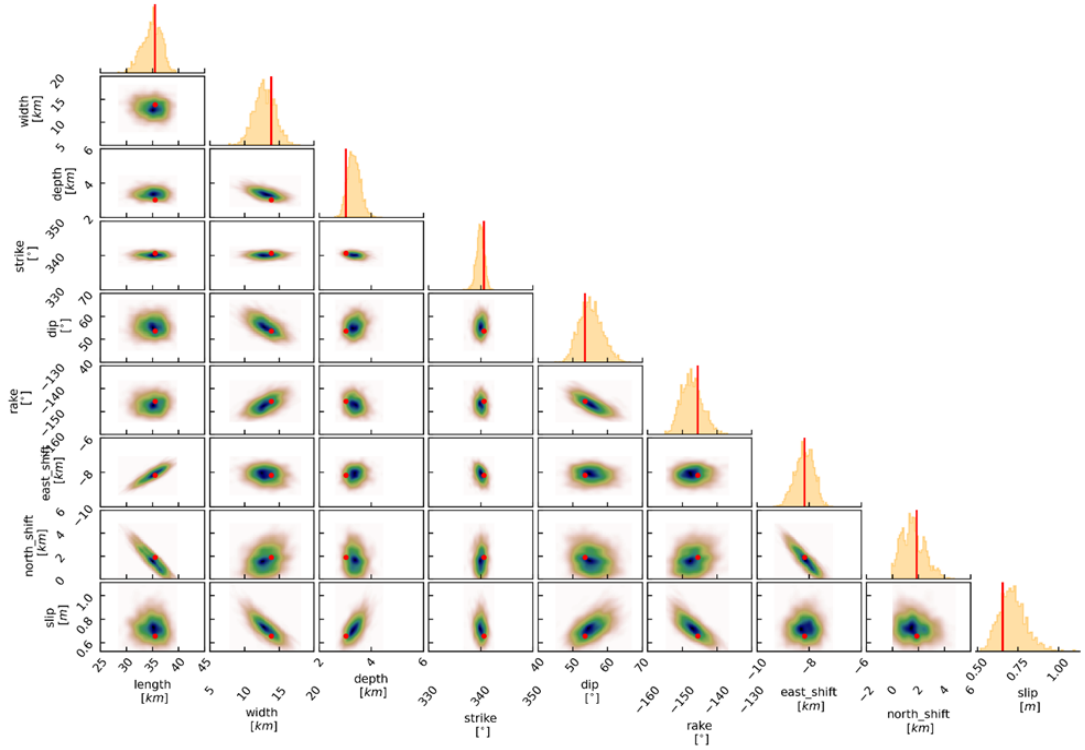

Fig. 4. Posterior probability distributions for the fault model parameters of the 2021 Hovsgol earthquake. Red lines and cycles represent the maximum-a-posteriori probability solution. Scatter plots are contoured according to frequency (cold colors for high frequency, warm colors for low frequency).

The optimal coseismic slip inversion results indicate that the 2021 Turt earthquake ruptured on a fault structure with a length of ~35 km (coseismic slip > 0.2m) along the west bank of Lake Hovsgol (Fig. 5), which successfully reproduces the InSAR observations (Fig. 3). The RMS of observations and model predictions are about 1 cm for InSAR observations. The coseismic slip is mainly concentrated at depths of 2-10 km with a peak slip of 1.2 m located at 7 km depth. The uncertainty of slip on each patch is marked by ellipses in Fig. 5. Assuming the average shear moduli is 34 GPa in the Hovsgol region (Laske et al., 2013), we calculated a geodetic moment (M_0) as ~2.46×10^{19} Nm. The estimated geodetic moment is corresponding to M_w 6.75, which is generally consistent with different catalogs (Table 1). Interestingly, the finite coseismic fault slip reveals that the slip is characterized by comparable dip-slip and right-lateral slip component (rake = -146°). In addition, no obvious shallow (0-2

km in depth) coseismic slip may indicate the shallow slip deficit (Xu et al., 2019).

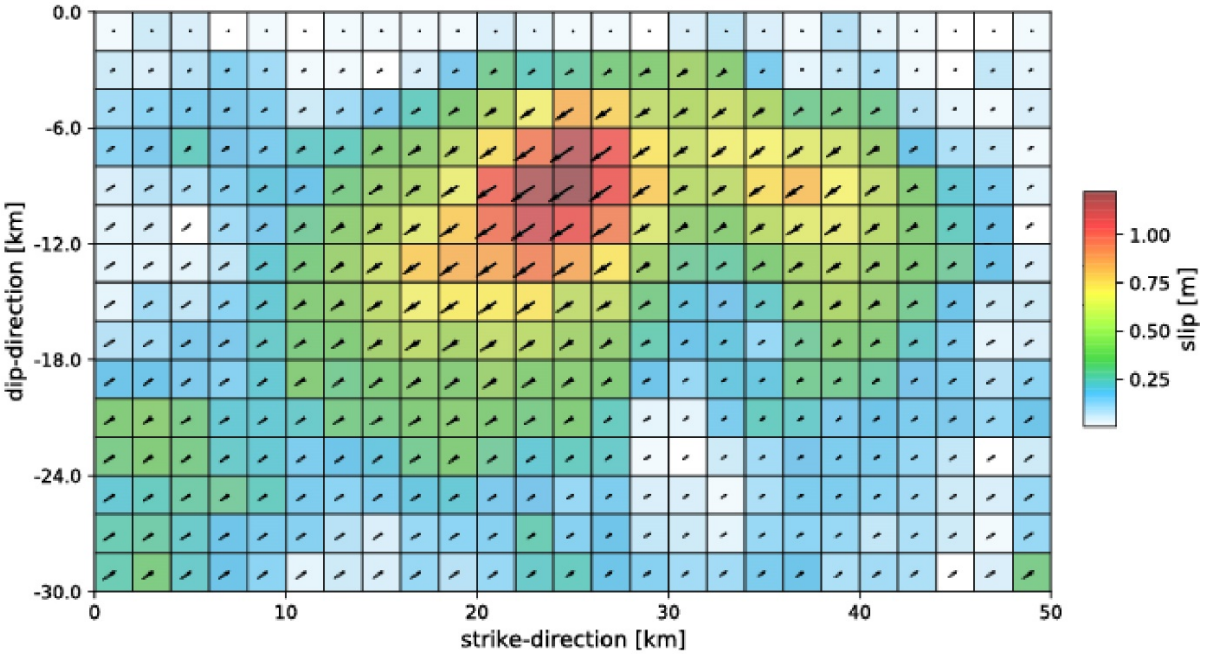

Fig. 5. Coseismic slip distribution solution for the 2021 Turt earthquake estimated using InSAR interferogram. The color patches and black arrows show the value and direction of the maximum-a-posterior solution. The two-sigma confidence interval is indicated by black ellipses around the arrow tips.

3.3. Stress inversion

The achieved stress inversion results are reported and summarized in Fig. 6 and Table 2, showing the stress fields in and around the Hovsgol basin is rather complicated. The sub-horizontal σ_1 axes in North Hovsgol Region (NHR) with NE-SW orientation and a low R (0.3) value indicating slightly difference in magnitude between σ_1 and σ_2 (Fig. 6b), coupled with horizontal σ_3 (Table 2), implies the NHR is under coexistence of both normal and strike slip stress regimes. The NHR is characterized by well-defined 95% confidence regions of sub-horizontal principal stress σ_3. In addition, we inverted all the compiled focal mechanisms for average stress filled in and around Hovsgol basin (Fig. 6a and c). It is similar to the stress filed of NHR but with much large average misfit angle 57°, indicating the background tectonics stress fields in and around Hovsgol basin are highly heterogenous (Michael, 1991).

Table 2. Stress tensor parameters as obtained from focal mechanisms inversion

Subregions	N[a]	σ_1 (°) az./pl.[b]	σ_2 (°) az./pl.	σ_3 (°) az./pl.	R	α(°)	Stress Regime	SHmax[c]
North Hovsgol	15	223/48	34/42	128/4	0.30	43	NS	38
Total region	29	250/45	32/38	138/20	0.34	57	NS	48

[a] Number of focal mechanisms; [b] Azimuth and plunge angles; [c] maximum horizontal compressive stress orientation.

According to the scheme of stress regime characterization and maximum horizontal compressive stress orientation (SHmax) proposed by (Zoback, 1992) based on the plunge and azimuth angles of stress axes, the results for the NHR and the entire study region show that it is under transtension stress field. The estimated SHmax in the 2021 Turt earthquake region is 38° (Table 2). This is consistent with our observed transtensional fault slip (Fig. 5) and comparable with the data (SHmax 23°/31°) from World Stress Map project (Heidbach et al., 2016).

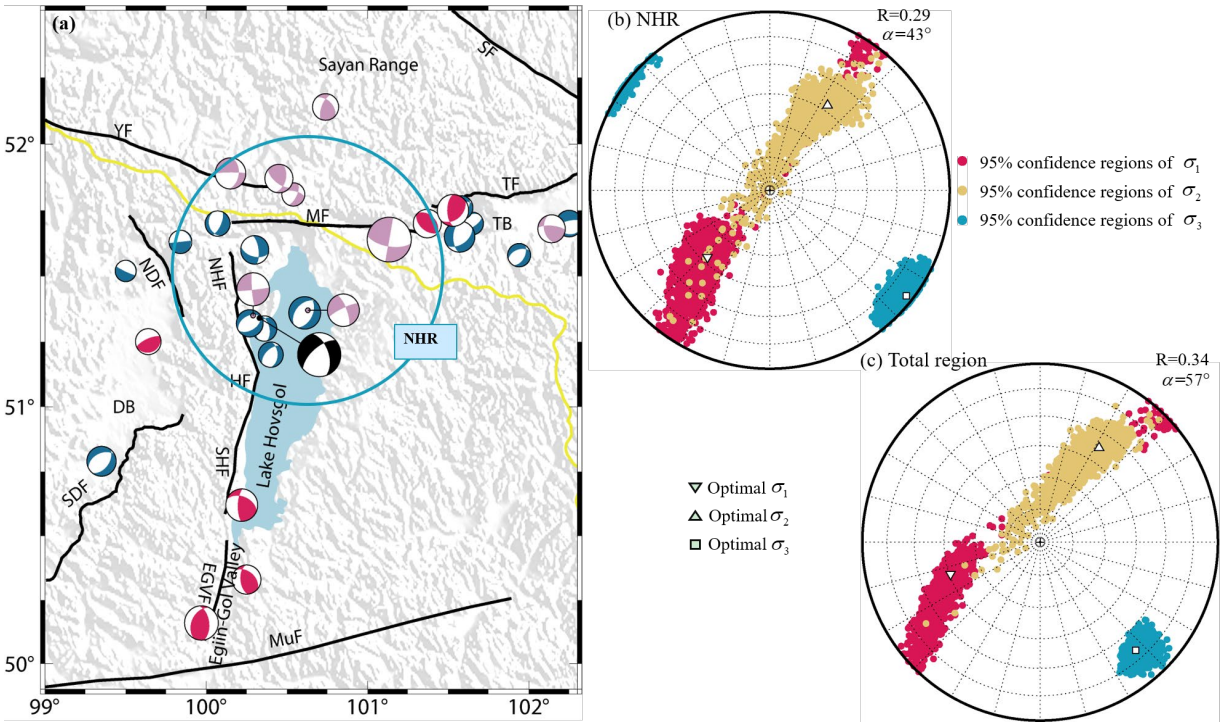

Fig. 6. The stress tensor inversion. (a) Focal mechanisms in the lower hemisphere projection used in the stress inversion for the entire region and for the northern part of the Hovsgol basin; (b) results of stress inversion for the northern part of the Hovsgol area; (c) results of stress inversion for the entire region.

4. Discussion

4.1. Faulting and stress heterogeneity in the Hovsgol basin region

The 2021 Mw 6.7 Turt earthquake is the largest instrumentally recorded event occurred within the Hovsgol basin. It is supposed to be caused by movement on the NW striking plane resulting from normal faulting with a right-lateral strike-slip component. The solution obtained in our study is in agreement with tensor moments issued by GCMT and IPGP, while other available solutions show mostly normal faulting (Fig. 1b and Table 1). The type of displacement in our focal mechanism corresponds to the kinematics of the NW fault determined from geological-structural data (Sankov et al., 2004). The field data described in (Sankov et al., 2004) also show, along with facets characterizing normal fault movements, regular right-lateral shear displacements of high-order stream valleys and asymmetric fanning cones. The stress regime deduced from the mainshock and previous focal mechanisms is transtension (Table 2); while earlier it was defined as pure extensive (Delouis et al., 2002). Since the stress inversion results are highly dependent on the input events, we argue that the completer and more up-to-date catalog in our study provide a more compelling evidence. Thus, we can state that the northern part of the Hovsgol basin is under extensional conditions with a right strike-slip component on NW oriented faults. This extension seems to be local because it is surrounded by transpression and strike-slip stress regimes (Delouis et al., 2002; Melnikova et al., 2004; Radziminovich et al., 2016; Sankov et al., 2004). Spatially, the present-day stress field in the region is changing from compression in the southern part of the Hovsgol basin to extension in its northern part, and then, to the north of the Hovsgol basin, the stress field is transpressive (Delouis et al., 2002; Melnikova et al., 2004; Radziminovich et al., 2016; Sankov et al., 2004). This complex spatial stress regime transition is probably responsible for the large average misfit angle in the stress inversion for the entire considered region (Fig.5, Table 2).

This indicates the complicated stress heterogeneity within the Hovsgol region, which can be deduced from the stress inversion results in and around the Hovsgol basin (Fig. 6). It is also visible from the basin morphology which shows a widespread deforming zone in the north but relatively narrow rift in the south (Fig. 7). Specifically, the topography is relatively lower in the southern counterpart. Gravity data also indicates remarking sedimentary thickness difference between north and south of the Hovsgol depression, with the maximum

550 m of sediments confined to the northern part of the depression, while the thickness of sediments rarely exceeds 350 m in the southern part of the Lake Hovsgol (Gladkochub and Donskaya, 2009; Zorin et al., 1989).

Reasons for heterogeneity of the stress field in the region are still under discussion. The local extension, for example, was modeled as opening of the northern basin which is in a T-shape conjunction of the Mondy fault and Hovsgol fault, and the diagonal NW fault forms the block structure of this area (Sankov et al., 2004). After the Turt earthquake, most of aftershocks (~60,000 in the first three months) from local seismic stations, are located in the conjugate angle region between near E-W MF and NW-S NHF, confirming activity of this block of the crust. In addition, stress heterogeneity including stress orientations and concentrations is attributed to active fault structures (Petit et al., 1996; Wilson et al., 2009; Yale, 2003) and contrasting rheology (Wileveau et al., 2007). Petit et al. (Petit et al., 1996) suggest that inherited structures have a crucial influence on the local stress field changes within the Baikal rift zone, so that changes in stresses are spatially confined to changes in the Siberian craton boundary. The sudden fault strike changes from near E-W direction (YF, MF and TF) to near N-S direction (HF, NDF and SDF), and then to NEE-SWW (MuF) orientation is observed in the Hovsgol region (Fig. 1b, Fig. 7), which may geometrically control the stress heterogeneity from north to south here.

Fault strike change is observed also along the western side of the Hovsgol basin, from SHF (10°) to NHF (341°). According to some study (Nicol et al., 2005; Wilson et al., 2009), the fault linkage point may control the displacements on the faults, so this change along the Hovsgol fault may inhibit the rupture propagation to SHF, confirming by the coseismic displacement mainly confined surrounding NHF during the Turt earthquake (Fig. 3). In this regard, it should be noted that seismicity of the instrumental period is concentrated in the northern part and southern tip of the Lake Hovsgol, while the south-central part of the lake (50.5° N - 51° N) seems to be a seismic gap where few earthquakes have been recorded (Dugarmaa et al., 2002; Radziminovich et al., 2016) (Fig.1).

4.2. Half-graben-dominated depression

Hovsgol basin is generally considered as the result of subsidence on the down-dropped block of half-graben with the master steep western HF hosting the 2021 mainshock. Some

literature only propose the active western major HF which is clear on the topography and geomorphology (Ivanov et al., 2015; Pollitz et al., 2003; Ritz et al., 2018). Some others, however, show the eastern minor Hovsgol fault (Petit et al., 1996; Tapponnier and Molnar, 1979; Wang et al., 2013). This makes it confused whether Hovsgol basin is dominated by half- or full-graben. Our geodetic observations show a dominated subsidence observed near the major HF on the western side indicating that the current subsidence is dominated by half-graben depression (Fig. 3). Epicenter distribution of the previous seismicity (Dugarmaa et al., 2002), as well as aftershocks following the 2021 Turt earthquake show that much intense seismic activities is observed on the west side of Lake Hovsgol compared with the east side.

Lithology of the basin sides differs; Pliocene basalts are located on the eastern side of HF, while it is relatively complex with sedimentary volcanic units (Riphean), Oselkovaya sedimentary series (Early Vendian) and Dzhidinsky sedimentary sequence (Middle Cambrian) on the western side (Fig. S3, http://bic.iwlearn.org/en/atlas/atlas-of-the-baikal-basin-eng/view). Bathymetry data of Lake Hovsgol indicates that the slope of the bottom of the lake is steep on the west and gentle on the east (Fig. 7), which is consistent with the observed fault scarps and steep slope on the west. This is also consistent with the west dome-blocky uplift and east arch-like structure features within Hovsgol basin (Gladkochub and Donskaya, 2009). Thus, the dominated west InSAR subsidence zone and remarkable difference of lithology, seismic activity, lake bathymetry, geomorphology fault scarps indicate that the current Hovsgol basin is still dominated by half-graben. Interestingly, the coseismic InSAR observations also show surface displacement on eastern Lake Hovsgol bank (Fig. 3), implying the potential local structures. Aftershocks from local seismic stations show microearthquake (ML ~2) cluster which agrees well with the displacement zone on eastern bank of Lake Hovsgol. These indicate that the minor structure may be activated by the 2021 Turt earthquake (Fig. 7b).

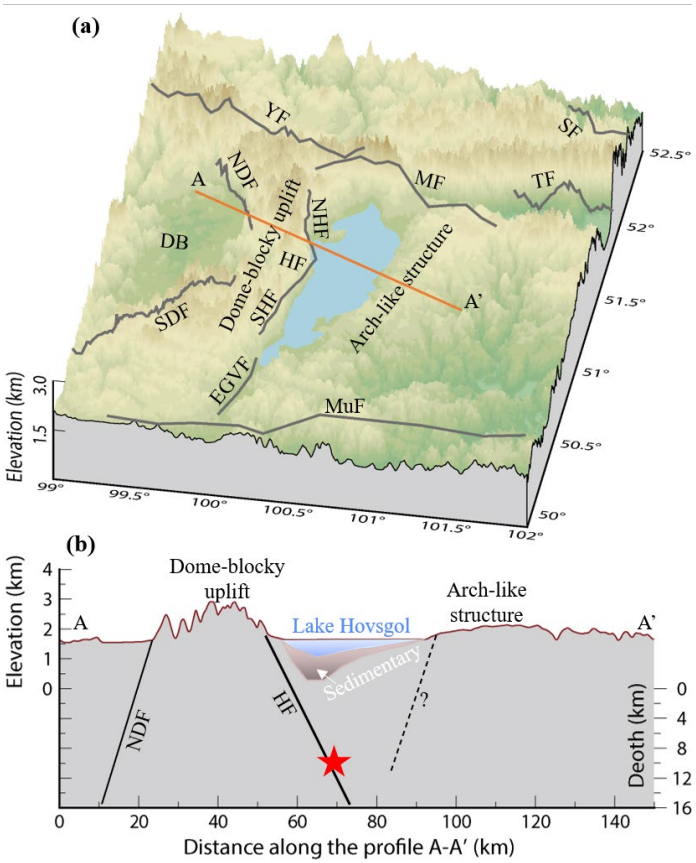

Fig. 7. Topography of the region. (a) The 3D view of topography in Fig. 1b. Gray lines represent active faults. The fault abbreviations are identical to those in Fig. 1. Orange line is the profile A-A' shown in (b). (b) The 2D conceptional model on the profile A-A'. Solid and dashed black lines represent the seismogenic fault and a possible oppositely dipping fault beneath the eastern bank of Lake Hovsgol. Red star indicates the hypocenter of the 2021 Turt earthquake.

4.3. Regional Seismic Hazard

Considering the complicated heterogeneity stress background in the Hovsgol region, it is crucial to evaluate the influence of 2021 Turt earthquake on its surrounding active faults. Seismic stress triggering theory indicates that accumulated tectonic stress is suddenly released during earthquakes, the redistributed stress may influence the adjacent faults with stress triggers promoting the subsequent seismicity or stress shadows delaying the subsequent earthquake ruptures (Harris, 1998; King et al., 1994; Stein et al., 1994). Utilizing the coseismic slip model caused by the 2021 Turt earthquake as the driving source, and assuming the effective coefficient of μ=0.4, we estimated the static Coulomb Failure Stress changes (ΔCFS)

triggered by the mainshock on the surrounding active faults (Lin and Stein, 2004; Toda et al., 2005).

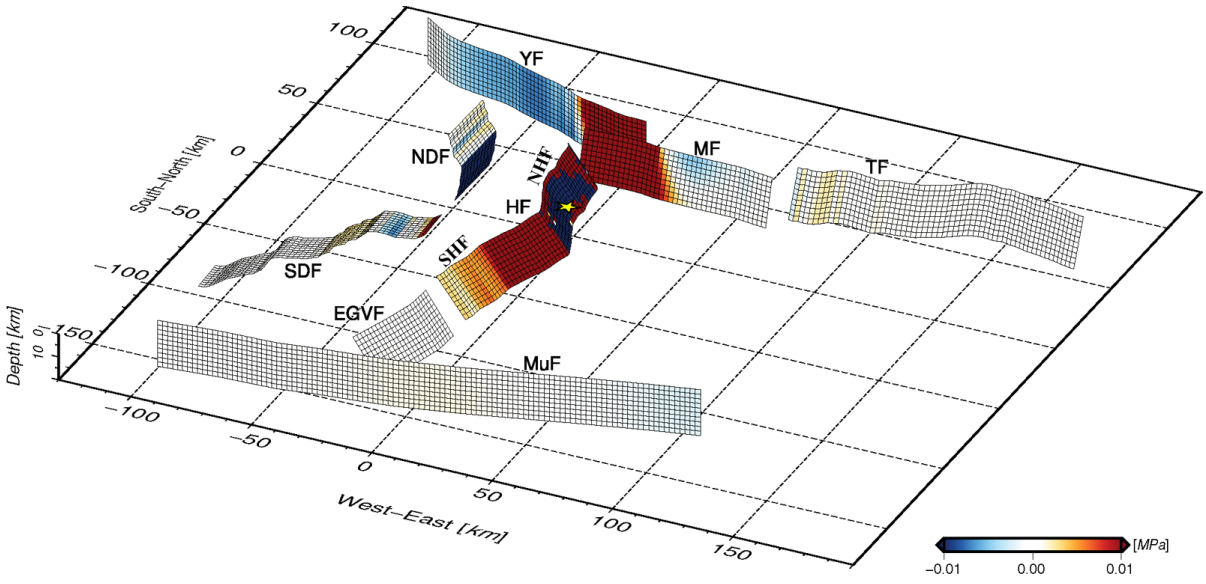

Fig. 8. Distribution of the static ΔCFS in the adjacent active faults induced by the 2021 Turt earthquake. The fault abbreviations are identical to those in Fig. 1b. Yellow star represents the USGS hypocenter. The geometries of the receiver faults are determined based on the information of regional moment tensor and GEM Global Active Faults (Table S4).

The maximum positive and negative static ΔCFS both about 2.5 MPa are found on the NHF (Fig. 8 and Fig. S4). It is worth noting that color scale is saturated at [-0.01 0.01] MPa for the visualization (Fig. 8). Strong stress triggers around coseismic rupture zone on NHF may explain the aftershocks after the mainshock and indicates potential postseismic transients (e.g., afterslip, poroelastic rebound, and viscoelastic relaxation). Stress triggers (0.16 MPa, Fig. 8 and Table S4) are found on the west Mondy Fault, a sinistral strike slip fault dipping south which hosted the 1950 Mondy Mw 6.9 (Delouis et al., 2002). In addition, 0.03 MPa stress triggers are observed on the east tip of YF (Fig. 8 and Table S4); whereas the NDF, west YF and east MF are mainly located in a stress shadow zone. It is obviously that the geometries of receiver faults play an important role in the ΔCFS calculations. For instance, the striking orientation changes are significantly influence the polarity (stress triggers or stress shadows) of ΔCFS, which can be observed clearly on fault NDF and SDF (Fig. 8). This kind of structure-orientation-related ΔCFS polarity is also reported, for example, in the case of 2020 Mw 6.5 Monte Cristo Range Earthquake (Zheng et al., 2020). This seems further confirming

that the strikes change is one of the potential reasons for the stress heterogeneity in Hovsgol region. The calculated positive ΔCFS on the northward faults (east YF, west MF and central MuF) exceeds the earthquake triggering threshold 0.01 MPa (Hardebeck et al., 1998). This indicates that the seismic hazard for these faults may be potentially increased, especially for the West Mondy Fault. Besides, rather strong positive ΔCFS (~0.5 MPa, Fig. 8 and Table S4) are observed on the SHF induced by the 2021 Turt earthquake. Considering that the SHF is a seismic gap during the instrumental era, we suggest that potential seismic hazard on SHF should be also taken into consideration.

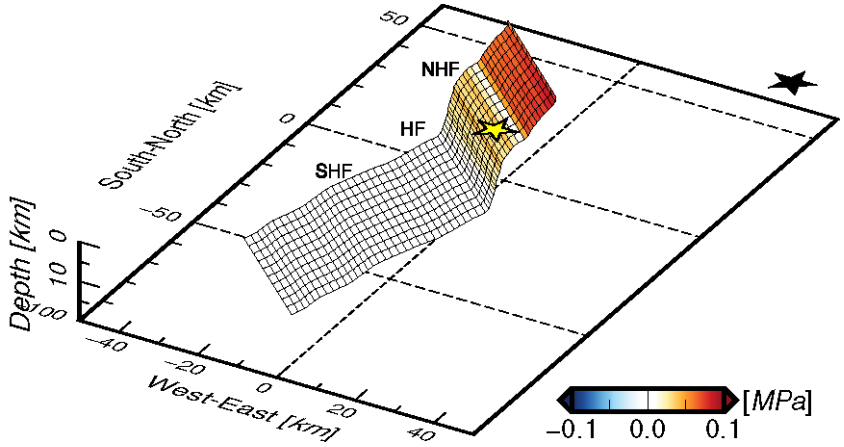

Fig. 9. Distribution of the static ΔCFS on the Hovsgol Fault induced by the 1950 Mondy Mw 6.9 earthquake. The effective friction coefficient is 0.4. The fault abbreviations are identical to those in Fig. 1b. Yellow and black stars represent the hypocenter of 2021 Turt earthquake and 1950 Mondy earthquake, respectively.

In addition, considering that the 1950 Mondy Mw 6.9 and the 2021 Turt Mw 6.7 earthquakes are only ~70 km apart, we modeled the possible impact of the Mondy fault. Based on the focal mechanism of 1950 Mondy earthquake (Delouis et al., 2002), we synthesized the uniform pure sinistral coseismic slip (0.83 m) on a 50 km×20 km fault plane with strike 100° and dip 75°. With the same method above, the static Coulomb Failure Stress changes (ΔCFS) triggered by the 1950 Mondy earthquake were estimated on the Hovsgol Fault (Figs. 9 and S5). Almost all positive static ΔCFS with an average value of 0.05 MPa are located on the NHF, indicating that the 1950 Mondy event may significantly promote the 2021 Turt earthquake. Given the average stress drop of about 0.72 MPa in the 2021 rupture zone and assuming recurrence earthquake releasing the same tectonic stress, we suggest that the 1950 event advanced the 2021 earthquake by about 7% recurrence interval. However, it seems to

have little positive effect on SHF and shows stress shadow with a peak value of -0.008 MPa inhibiting earthquake nucleation on the north tip of the SHF (Figs. 9 and S5). This may explain, to some degree, the seismic gap on SHF and seems to evidence again that structures geometry plays a significant role in local stress field.

5. Conclusions

In this study, we investigated the seismogenic fault geometry, coseismic fault slip with surface displacement fields for the Mw6.7 2021 Turt earthquake by using InSAR and teleseismic data. We found that the observations can be best explained by the fault slip on a seismogenic fault with a strike of 341° and a dip angle of 54°. Coseismic slip is characterized by normal faulting with a dextral strike-slip component with a peak value of 1.2 m at 7 km depth. According to InSAR data, up to ~20 cm surface subsidence occurred at the hanging wall of the fault. The stress inversion results show that this earthquake occurred within a transtensive stress regime. It is a local area with such a regime being surrounded by transpressive and strike-slip stress fields. This stress heterogeneity is probably controlled by the distinct structure geometries in and around Hovsgol basin.

The dominated west bank InSAR subsidence and remarkable difference of lithology, seismic activity, lake bottom slope, geomorphology fault scarps, indicate that the current Hovsgol basin is still dominated by half-graben. The calculated ΔCFS induced by the 2021 Turt earthquake suggests the potential seismic hazard associated with the West Mondy Fault that deserves further attention. In addition, the ΔCFS caused by the 1950 Mondy earthquake may advance the 2021 Turt earthquake by ~7% recurrence interval. The findings reported here have important implications for regional heterogenous stress field of the crust, graben deformation mechanisms and seismic potential.

Acknowledgement

We thank Editor * and * anonymous reviewers for their constructive reviews and comments. This work was supported by the National Key R&D Program of China (2019YFC1509205), by the National Natural Science Foundation of China (No. 41804015).

Author Contributions

X.L. and W.X. designed the study, organized experimental work. X.L. wrote the original manuscript. X.L. and N.F. conducted the experimental work. X.L., W.X. and N.A.R. led the writing of the manuscript with contributions from all coauthors. All authors commented on, reviewed, and edited the presented version of manuscript.

Competing Interests

The authors declare that they have no competing interests.

Data Availability Statement

Raw Sentinel-1A data are available from https://scihub.copernicus.eu/dhus/#/home. Seismic data are accessed from IRIS (https://ds.iris.edu). The processed data used in the study are available (https://doi.org/10.5281/zenodo.5078988). The GAMMA commercial software is obtained from https://www.gamma-rs.ch/software. The BEAT software is obtained from https://github.com/hvasbath/beat. The iterative joint stress inversion software is obtained from https://www.ig.cas.cz/en/stress-inverse/. The Coulomb3 software is available from https://www.usgs.gov/software/coulomb-3. The Generic Mapping Tools (Wessel et al., 2013) created figures are obtained from https://www.genericmapping-tools.org/.

References

Bayasgalan, A., Jackson, J., McKenzie, D., 2005. Lithosphere rheology and active tectonics in Mongolia: relations between earthquake source parameters, gravity and GPS measurements. Geophysical Journal International 163, 1151-1179.

Calais, E., Vergnolle, M., San'kov, V., Lukhnev, A., Miroshnitchenko, A., Amarjargal, S., Déverchère, J., 2003. GPS measurements of crustal deformation in the Baikal-Mongolia area (1994-2002): Implications for current kinematics of Asia. Journal of Geophysical Research: Solid Earth 108.

Chen, C.W., Zebker, H.A., 2001. Two-dimensional phase unwrapping with use of statistical models for cost functions in nonlinear optimization. Journal of the Optical Society of America a-Optics Image Science and Vision 18, 338-351.

Del Moral, P., Doucet, A., Jasra, A., 2006. Sequential monte carlo samplers. Journal of the Royal Statistical Society: Series B (Statistical Methodology) 68, 411-436.

Delouis, B., Déverchère, J., Melnikova, V., Radziminovitch, N., Loncke, L., Larroque, C., Ritz, J., San'kov, V., 2002. A reappraisal of the 1950 (Mw 6.9) Mondy earthquake, Siberia, and its relationship to the strain pattern at the south-western end of the Baikal rift zone. Terra Nova 14, 491-500.

Dobrynina, A.A., Sankov, V.A., Tcydypova, L.R., German, V.I., Chechelnitsky, V.V., Ulzibat, M., 2018. Hovsgol earthquake 5 December 2014, MW = 4.9: seismic and acoustic effects. Journal of Seismology 22, 377-389.

Dugarmaa, T., Schlupp, A., Adija, M., Ankhtsetseg, D., Bayar, G., Munkhuu, D., Selenge, L., Tsembel, B., Ulziibat, M., Odonbaatar, C., 2002. Seismic Map of Mongolia and Site Effect Microzoning at the Capital, Ulaanbaatar, AGU Fall Meeting Abstracts, pp. S71B-1100.

Farr, T.G., Rosen, P.A., Caro, E., Crippen, R., Duren, R., Hensley, S., Kobrick, M., Paller, M., Rodriguez, E., Roth, L., Seal, D., Shaffer, S., Shimada, J., Umland, J., Werner, M., Oskin, M., Burbank, D., Alsdorf, D., 2007. The shuttle

548 radar topography mission. Reviews of Geophysics 45.
549 Gephart, J.W., Forsyth, D.W., 1984. An improved method for determining the regional stress tensor using
550 earthquake focal mechanism data: application to the San Fernando earthquake sequence. Journal of
551 Geophysical Research: Solid Earth 89, 9305-9320.
552 Gladkochub, D., Donskaya, T., 2009. Overview of geology and tectonic evolution of the Baikal-Tuva area,
553 Biosilica in Evolution, Morphogenesis, and Nanobiotechnology. Springer, pp. 3-26.
554 Hardebeck, J.L., Nazareth, J.J., Hauksson, E., 1998. The static stress change triggering model: Constraints
555 from two southern California aftershock sequences. Journal of Geophysical Research: Solid Earth 103,
556 24427-24437.
557 Harris, R.A., 1998. Introduction to Special Section: Stress Triggers, Stress Shadows, and Implications for
558 Seismic Hazard. Journal of Geophysical Research: Solid Earth 103, 24347-24358.
559 Heidbach, O., Rajabi, M., Reiter, K., Ziegler, M., 2016. WSM-World Stress Map Database Release. GFZ Data
560 Services. http//: doi. org/10.5880/WSM.
561 Ivanov, A.V., Demonterova, E.I., He, H., Perepelov, A.B., Travin, A.V., Lebedev, V.A., 2015. Volcanism in the
562 Baikal rift: 40years of active-versus-passive model discussion. Earth-Science Reviews 148, 18-43.
563 Jolivet, M., Arzhannikov, S., Chauvet, A., Arzhannikova, A., Vassallo, R., Kulagina, N., Akulova, V., 2013.
564 Accommodating large-scale intracontinental extension and compression in a single stress-field: A key
565 example from the Baikal Rift System. Gondwana Research 24, 918-935.
566 Jónsson, S., Zebker, H., Segall, P., Amelung, F., 2002. Fault slip distribution of the 1999 M w 7.1 Hector Mine,
567 California, earthquake, estimated from satellite radar and GPS measurements. Bulletin of the Seismological
568 Society of America 92, 1377-1389.
569 King, G.C., Stein, R.S., Lin, J., 1994. Static stress changes and the triggering of earthquakes. Bulletin of the
570 Seismological Society of America 84, 935-953.
571 Laske, G., Masters, G., Ma, Z., Pasyanos, M., 2013. Update on CRUST1. 0—A 1-degree global model of Earth's
572 crust, Geophys. Res. Abstr, p. 2658.
573 Li, Z., Ding, X., Huang, C., Zhu, J., Chen, Y., 2008. Improved filtering parameter determination for the
574 Goldstein radar interferogram filter. ISPRS Journal of Photogrammetry and Remote Sensing 63, 621-634.
575 Lin, J., Stein, R.S., 2004. Stress triggering in thrust and subduction earthquakes and stress interaction
576 between the southern San Andreas and nearby thrust and strike-slip faults. Journal of Geophysical
577 Research: Solid Earth 109.
578 Liu, X., Xu, W., 2019. Logarithmic model joint inversion method for coseismic and postseismic slip:
579 Application to the 2017 Mw 7.3 Sarpol Zahāb earthquake, Iran. Journal of Geophysical Research: Solid
580 Earth 124, 12034-12052.
581 Lund, B., Slunga, R., 1999. Stress tensor inversion using detailed microearthquake information and stability
582 constraints: Application to Ölfus in southwest Iceland. Journal of Geophysical Research: Solid Earth 104,
583 14947-14964.
584 Martínez-Garzón, P., Ben-Zion, Y., Abolfathian, N., Kwiatek, G., Bohnhoff, M., 2016. A refined methodology for
585 stress inversions of earthquake focal mechanisms. Journal of Geophysical Research: Solid Earth 121, 8666-
586 8687.
587 Melnikova, V.I., A., G.N., A.I., S., 2020. Catalogue of earthquake focal mechanisms for the Baikal region for
588 2014 In: Earthquakes of the Northern Eurasia, Obninsk, GS RAS
589
590 Melnikova, V.I., Radziminovich, N.A., Adyaa, M., 2004. Mechanisms of earthquake foci and seismotectonic
591 deformations of the Mongolia region. Complex geophysical and seismological investigations in Mongolia.
592 Research Centre of Astronomy and Geophysics of the Mongolian Academy of Sciences, Ulaanbaatar, 165-170.
593 Meltzer, A., Stachnik, J.C., Sodnomsambuu, D., Munkhuu, U., Tsagaan, B., Dashdondog, M., Russo, R., 2019. The

Central Mongolia Seismic Experiment: Multiple Applications of Temporary Broadband Seismic Arrays. Seismological Research Letters 90, 1364-1376.

Michael, A.J., 1984. Determination of stress from slip data: faults and folds. Journal of Geophysical Research: Solid Earth 89, 11517-11526.

Michael, A.J., 1987. Use of focal mechanisms to determine stress: a control study. Journal of Geophysical Research: Solid Earth 92, 357-368.

Michael, A.J., 1991. Spatial variations in stress within the 1987 Whittier Narrows, California, aftershock sequence: New techniques and results. Journal of Geophysical Research: Solid Earth 96, 6303-6319.

Nicol, A., Walsh, J., Berryman, K., Nodder, S., 2005. Growth of a normal fault by the accumulation of slip over millions of years. Journal of Structural Geology 27, 327-342.

Petit, C., Déverchère, J., 2006. Structure and evolution of the Baikal rift: A synthesis. Geochemistry, Geophysics, Geosystems 7.

Petit, C., Déverchère, J., Calais, E., San'kov, V., Fairhead, D., 2002. Deep structure and mechanical behavior of the lithosphere in the Hangai–Hövsgöl region, Mongolia: new constraints from gravity modeling. Earth and Planetary Science Letters 197, 133-149.

Petit, C., Déverchère, J., Houdry, F., Sankov, V.A., Melnikova, V.I., Delvaux, D., 1996. Present-day stress field changes along the Baikal rift and tectonic implications. Tectonics 15, 1171-1191.

Pollitz, F., Vergnolle, M., Calais, E., 2003. Fault interaction and stress triggering of twentieth century earthquakes in Mongolia. Journal of Geophysical Research: Solid Earth 108.

Radziminovich, N.A., Bayar, G., Miroshnichenko, A.I., Demberel, S., Ulziibat, M., Ganzorig, D., Lukhnev, A.V., 2016. Focal mechanisms of earthquakes and stress field of the crust in Mongolia and its surroundings. Geodynamics & Tectonophysics 7, 23-38.

Ritz, J., Larroque, C., Stephan, J., San'kov, V., Arjannikova, A., Calais, E., Deverchere, J., Loncke, L., 2000. When compression meets extension: interaction or competition? The example of the Tunka basin (Western Baikal, Siberia). Proceedings of the Geosciences, 122.

Ritz, J.F., Arzhannikova, A., Vassallo, R., Arzhannikov, S., Larroque, C., Michelot, J.L., Massault, M., 2018. Characterizing the Present-Day Activity of the Tunka and Sayan Faults Within Their Relay Zone (Western Baikal Rift System, Russia). Tectonics 37, 1376-1392.

Sankov, V.A., Microshnichenko, A.I., Parfeevets, A.V., Arzhannikova, A.V., Lukhnev, A.V., 2004. Late Cenozoic state of stress in the Earth's crust of the Khubsugul region (Northern Mongolia): Field and experimental evidence. Geotectonics 38, 142-152.

Sankov, V.A., Parfeevets, A.V., Lukhnev, A.V., Miroshnichenko, A.I., Ashurkov, S.V., 2011. Late Cenozoic geodynamics and mechanical coupling of crustal and upper mantle deformations in the Mongolia-Siberia mobile area. Geotectonics 45, 378-393.

Schlupp, A., Cisternas, A., 2007. Source history of the 1905 great Mongolian earthquakes (Tsetserleg, Bolnay). Geophysical Journal International 169, 1115-1131.

Stein, R.S., King, G.C., Lin, J., 1994. Stress triggering of the 1994 M= 6.7 Northridge, California, earthquake by its predecessors. Science 265, 1432-1435.

Tapponnier, P., Molnar, P., 1979. Active faulting and cenozoic tectonics of the Tien Shan, Mongolia, and Baykal Regions. Journal of Geophysical Research: Solid Earth 84, 3425-3459.

Toda, S., Stein, R.S., Richards-Dinger, K., Bozkurt, S.B., 2005. Forecasting the evolution of seismicity in southern California: Animations built on earthquake stress transfer. Journal of Geophysical Research: Solid Earth 110.

Vasiliev, E.P., Belichenko, V.G., Reznitskii, L.Z., 1997. Relationship between Ancient and Cenozoic structures at the Southwestern flank of the Baikal rift zone. Doklady Academii Nauk 353, 789-792.

Vasyura-Bathke, H., Dettmer, J., Steinberg, A., Heimann, S., Isken, M.P., Zielke, O., Mai, P.M., Sudhaus, H.,

640 Jónsson, S., 2020. The Bayesian earthquake analysis tool. Seismological Research Letters 91, 1003-1018.
641 Vavryčuk, V., 2014. Iterative joint inversion for stress and fault orientations from focal mechanisms.
642 Geophysical Journal International 199, 69-77.
643 Vavryčuk, V., Bouchaala, F., Fischer, T., 2013. High-resolution fault image from accurate locations and focal
644 mechanisms of the 2008 swarm earthquakes in West Bohemia, Czech Republic. Tectonophysics 590, 189-
645 195.
646 Vergnolle, M., Pollitz, F., Calais, E., 2003. Constraints on the viscosity of the continental crust and mantle from
647 GPS measurements and postseismic deformation models in western Mongolia. Journal of Geophysical
648 Research: Solid Earth 108.
649 Wald, D.J., Heaton, T.H., Hudnut, K.W., 1996. The slip history of the 1994 Northridge, California, earthquake
650 determined from strong-motion, teleseismic, GPS, and leveling data. Bulletin of the Seismological Society of
651 America 86, S49-S70.
652 Wang, M., Shen, Z.K., 2020. Present-Day Crustal Deformation of Continental China Derived From GPS and
653 Its Tectonic Implications. Journal of Geophysical Research: Solid Earth 125.
654 Wang, S., Pei, S., Xu, G., Gao, A., 2013. Pn velocity structure at the uppermost mantle of Mongolia and
655 neighboring regions. Chinese Journal of Geophysics 56, 4106-4112.
656 Warren-Smith, E., Fry, B., Wallace, L., Chon, E., Henrys, S., Sheehan, A., Mochizuki, K., Schwartz, S., Webb, S.,
657 Lebedev, S., 2019. Episodic stress and fluid pressure cycling in subducting oceanic crust during slow slip.
658 Nature Geoscience 12, 475-481.
659 Wegmuller, U., Werner, C., Stroozzi, T., Wiesmann, A., Frey, O., Santoro, M., 2015. Sentinel-1 support in the
660 GAMMA Software. ESASP 731, 33.
661 Wessel, P., Smith, W.H., Scharroo, R., Luis, J., Wobbe, F., 2013. Generic mapping tools: improved version
662 released. Eos, Transactions American Geophysical Union 94, 409-410.
663 Wileveau, Y., Cornet, F., Desroches, J., Blumling, P., 2007. Complete in situ stress determination in an argillite
664 sedimentary formation. Physics and Chemistry of the Earth, Parts A/B/C 32, 866-878.
665 Wilson, P., Hodgetts, D., Rarity, F., Gawthorpe, R.L., Sharp, I.R., 2009. Structural geology and 4D evolution of a
666 half-graben: New digital outcrop modelling techniques applied to the Nukhul half-graben, Suez rift, Egypt.
667 Journal of Structural Geology 31, 328-345.
668 Xu, G., Xu, C., Wen, Y., Yin, Z., 2019. Coseismic and Postseismic Deformation of the 2016 MW 6.2 Lampa
669 Earthquake, Southern Peru, Constrained by Interferometric Synthetic Aperture Radar. Journal of
670 Geophysical Research: Solid Earth 124, 4250-4272.
671 Xu, W.B., 2017. Finite-fault slip model of the 2016 M-w 7.5 Chiloe earthquake, southern Chile, estimated
672 from Sentinel-1 data. Geophysical Research Letters 44, 4774-4780.
673 Xu, W.B., Rivalta, E., Li, X., 2017. Magmatic architecture within a rift segment: Articulate axial magma storage
674 at Erta Ale volcano, Ethiopia. Earth and Planetary Science Letters 476, 79-86.
675 Yale, D.P., 2003. Fault and stress magnitude controls on variations in the orientation of in situ stress.
676 Geological Society, London, Special Publications 209, 55-64.
677 Zheng, A., Chen, X., Xu, W., 2020. Present-day deformation mechanism of the northeastern Mina deflection
678 revealed by the 2020 Mw 6.5 Monte Cristo Range earthquake. Geophysical Research Letters.
679 Zoback, M.L., 1992. First- and second-order patterns of stress in the lithosphere: The World Stress Map
680 Project. Journal of Geophysical Research 97.
681 Zorin, Y.A., Tumtanov, E.K., Arvisbaatar, N., 1989. Structure of Cenozoic basins of the Prekhubsugul region
682 from gravity data. Russian Geology and Geophysics 10, 130-136.
683

Supporting Information for

Coseismic Fault Slip and Transtensional Stress Field in the Hovsgol basin Revealed by the 2021 Mw 6.7 Turt, Mongolia Earthquake

Xiaoge Liu[1], Wenbin Xu[1,*], Natalia A. Radziminovich[2], Nan Fang[1], Lei Xie[3]

[1]School of Geosciences and Info-Physics, Central South University, Changsha 410083, Hunan, P.R. China

[2]Institute of the Earth's Crust, Siberian Branch of the Russian Academy of Sciences, Lermontov Str., 128, Irkutsk 664033, Russia

[3]The Department of Land Surveying and Geo-Informatics, The Hong Kong Polytechnic University, Hong Kong, China

Contents of this file

Figures S1 to S5

Tables S1 to S4

Introduction

This supporting information includes figures showing teleseismic data location (Fig. S1), comparison between the observed teleseismic P waves and the synthetic waveforms (Fig. S2), regional geology, and lithology map (Fig. S3), Coulomb stress change on surrounding active faults induced by 2021 Turt earthquake (Fig. S4) and stress triggers on Hovsgol Fault caused by 1950 Mw 6.9 Mondy earthquake (Fig. S5). We also include tables describing the moment tensors (Table S1), coseismic InSAR data information (Table S2), optimal fault geometry parameters and their searching intervals in the non-linear inversion (Table S3) and geometry parameters of receiver faults for Coulomb stress change calculation (Table S4).

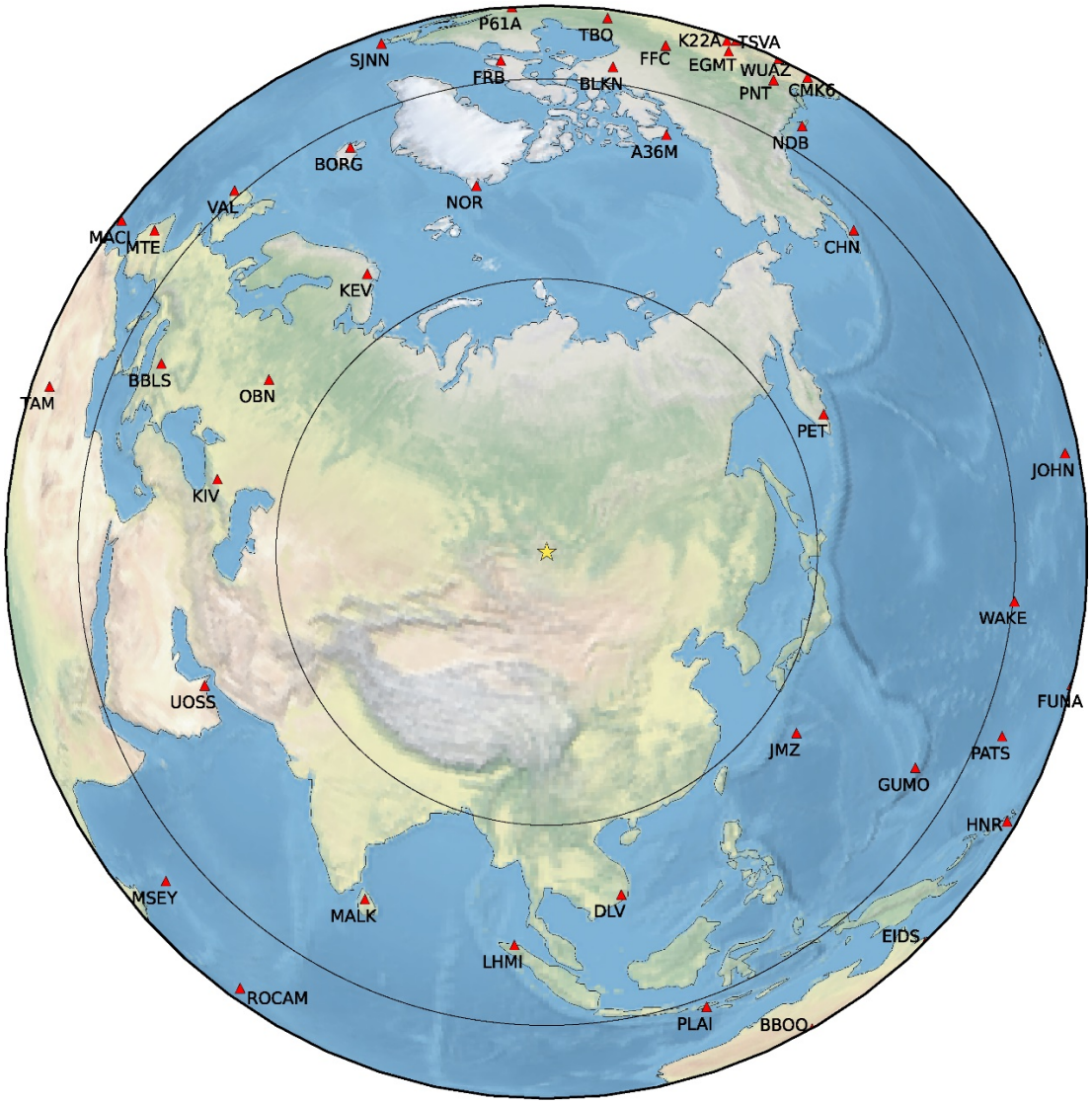

Fig. S1. Map in azimuthal equidistant projection centered on the epicenter of the 2021 Hovsgol earthquake (yellow star). Red triangles show the seismic stations that have been used in this study. The black circles mark the distances of 30, 60 and 90 degrees.

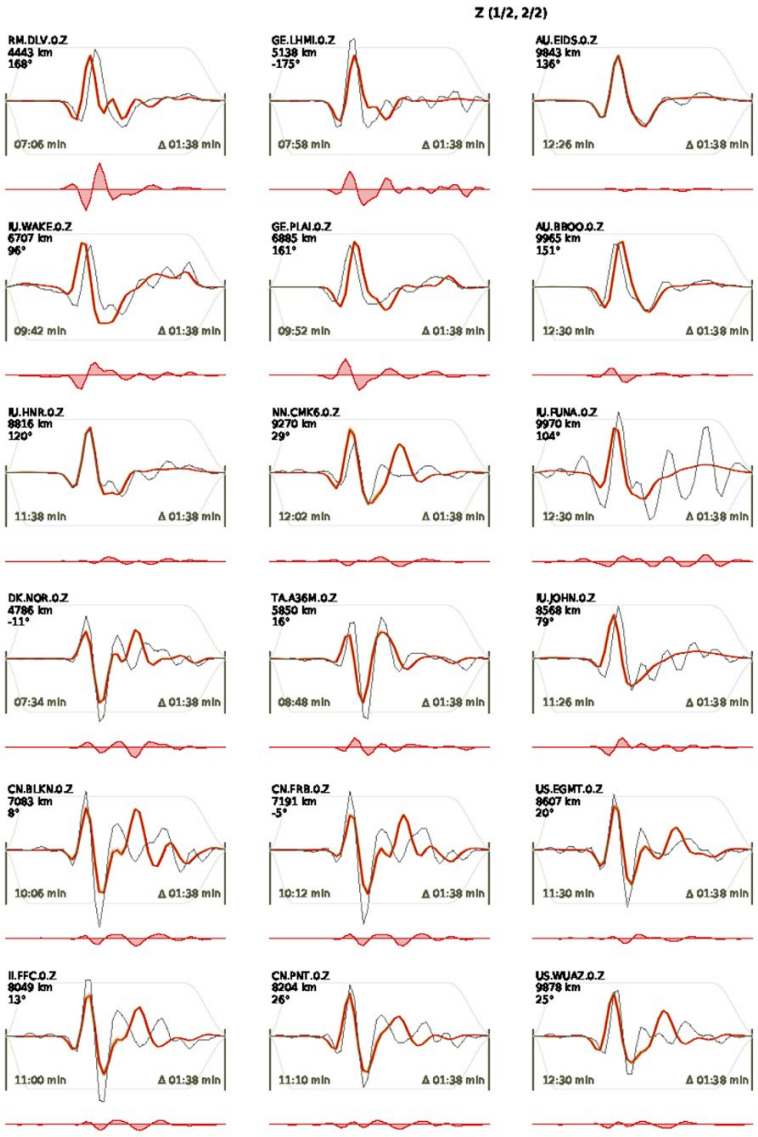

Fig. S2. Same as Fig. 2 but for other stations.

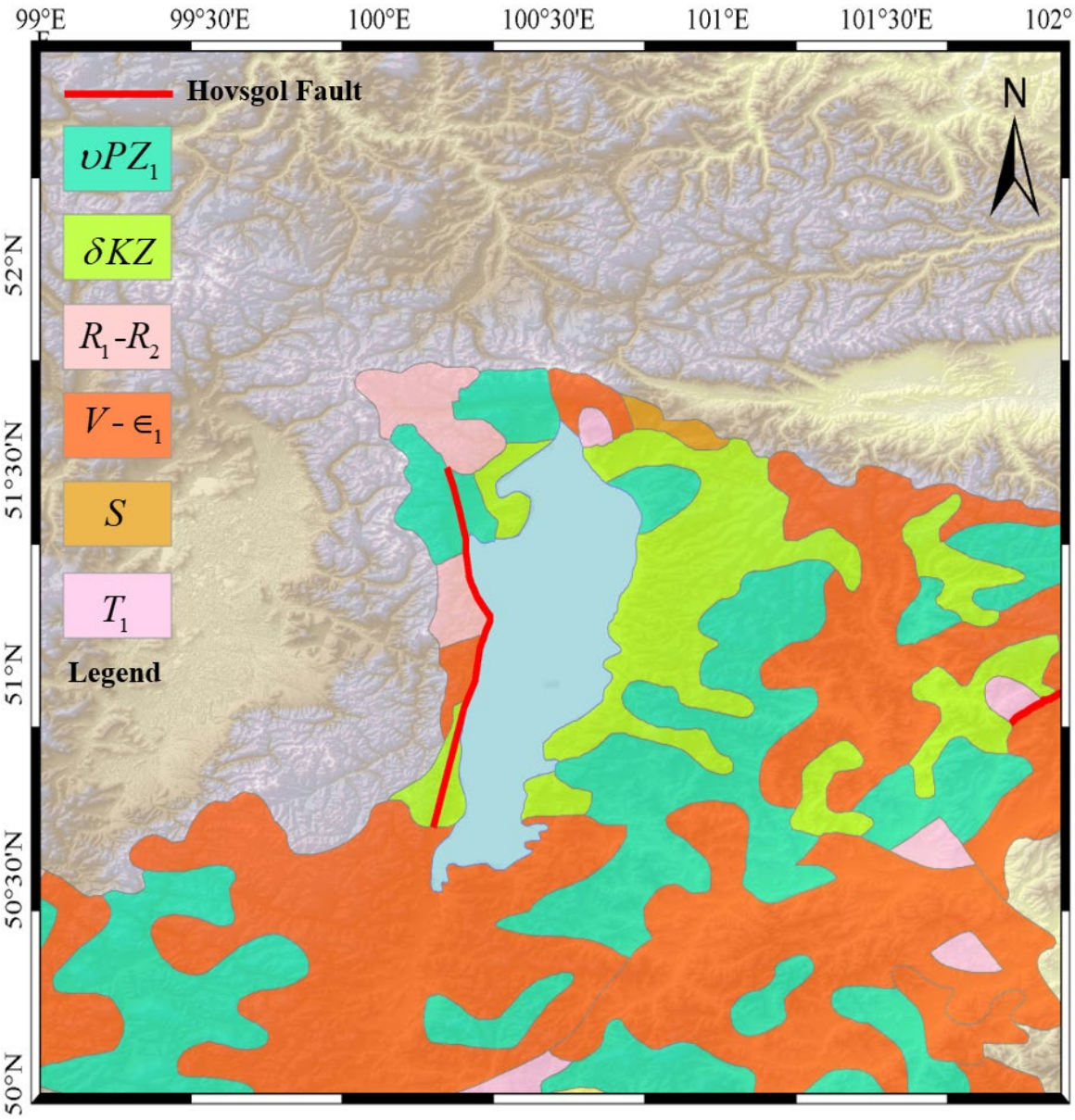

Fig. S3. The geology and lithology map are adopted from Atlas of the Hovsgol basin. υPZ_1: Dzhidinsky sedimentary sequence – gabbro, gabbro-norite, norite, diabase (Middle Cambrian); δKZ: Basalts (Pliocene); R_1-R_2: Sedimentary volcanic units (Middle Riphean); V-$\in_1$: Sedimentary volcanic units (Early Cambrian); S: Sedimentary volcanic units (Silurian); T_1: Chernoyarovskay suite - basic rocks, tuffaceous conglomerates, tuffaceous and stones. (Early-Middle Triassic). Detail lithology and geology information can be found from http://bic.iwlearn.org/en/atlas/atlas-of-the-baikal-basin-eng/view.

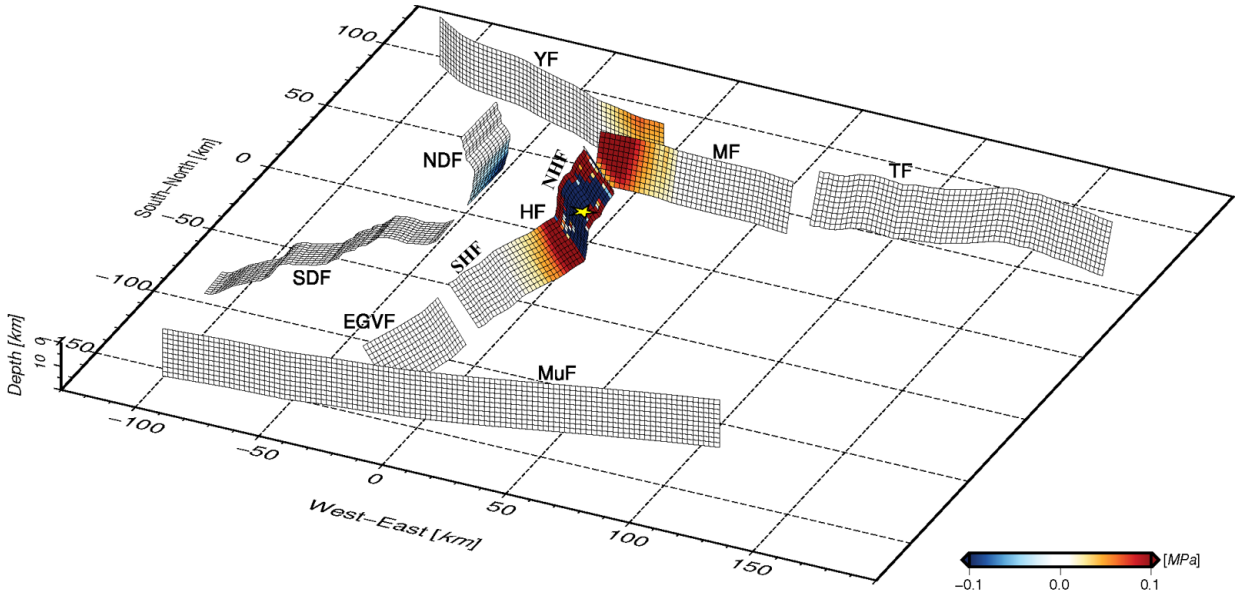

Fig. S4. Same as Fig. 8 but color scale saturated at [-0.1, 0.1] MPa

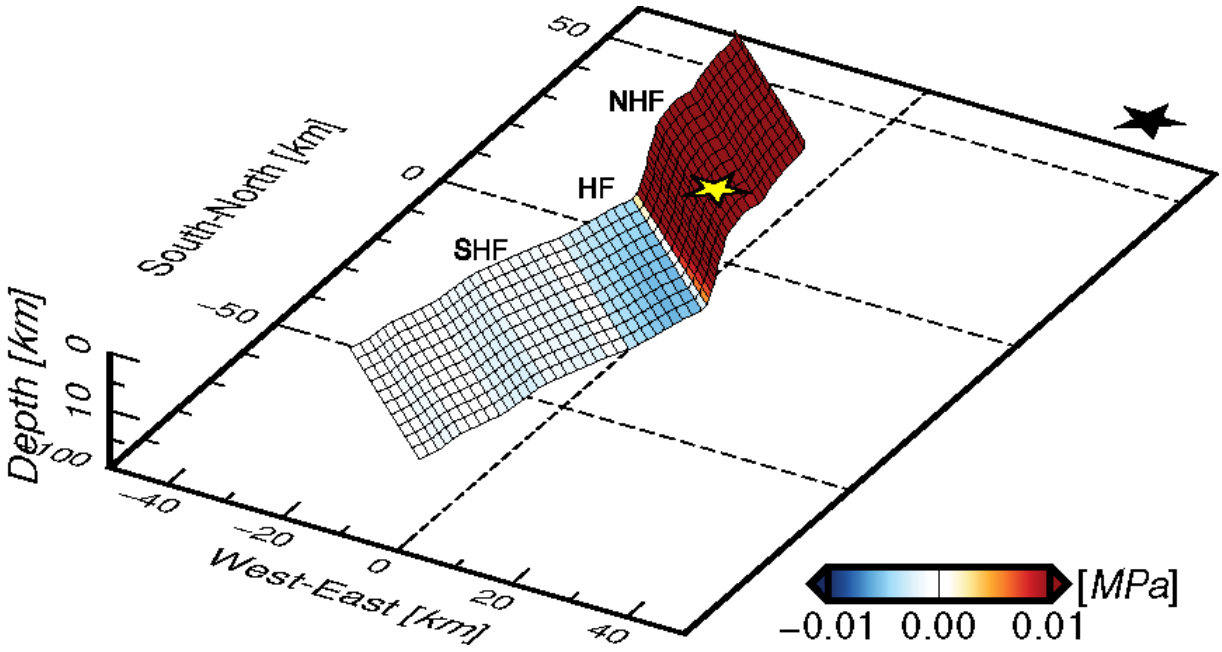

Fig. S5. Same as Fig. 9 but color scale saturated at [-0.01, 0.01] MPa

Table S1. Fault plane solutions for earthquakes in the Hovsgol area. Earthquakes with multiple focal mechanism solutions are highlighted in bold.

dd/mm/yyyy	Hour	Lat.	Lon.	Mag.	T pl	T az	N pl	N az	P pl	P az	Strike	Dip	Slip	Strike	Dip	Slip	reference
04/04/1950	18:44	51.8	101	Mw6.9	11	324	74	190	11	56	100	75	0	10	90	165	Delouis et al., 2002
21/12/1961	16:02	51.6	100.3	4.4	10	52	41	151	47	311	353	67	-44	104	50	-149	Khilko et al., 1985
29/08/1964	20:55	51.52	99.5	3.3	39	209	4	116	51	21	115	84	-94	329	7	-56	Khilko et al., 1985
01/04/1976	**19:02**	**50.62**	**100.22**	**5**	**77**	**132**	**13**	**306**	**2**	**36**	**293**	**48**	**72**	**139**	**45**	**109**	Khilko et al., 1985
01/04/1976	**19:02**	**50.62**	**100.22**	**5**	**46**	**137**	**41**	**344**	**14**	**242**	**182**	**70**	**133**	**292**	**47**	**28**	Golenetskii, 1980
14/03/1980	21:34	51.87	100.45	4.4	49	350	39	151	9	249	16	50	146	129	65	45	Khilko et al., 1985
03/12/1982	05:16	51.7	101.37	4.4	84	16	3	132	5	222	130	50	87	315	40	94	Golenetskii, 1986
06/04/1985	05:32	51.36	100.61	5	3	123	10	34	80	229	25	48	-102	223	44	-77	Solonenko et al. 1993
24/08/1985	22:57	51.2	100.4	3.9	6	295	24	28	64	190	0	44	-126	225	56	-60	Solonenko et al., 1993
08/03/1987	05:16	51.3	100.36	3.9	7	96	22	4	66	204	348	56	-117	210	42	-57	Solonenko et al., 1993
04/03/1989	19:43	50.79	99.35	4.6	2	140	14	50	76	236	37	48	-109	244	45	-70	Filina, 1993
05/02/1992	10:57	50.16	99.97	5.3	72	206	17	6	6	98	206	42	116	353	53	69	Melnikova, Radziminovich, 1998
13/01/1993	05:18	51.68	102.14	4.3	44	141	42	291	16	34	167	46	155	275	72	46	Melnikova, Radziminovich, 1998
02/09/1997	15:35	51.7	101.65	3.5	21	143	7	236	68	342	58	66	-83	221	25	-105	Melnikova, Radziminovich, 2003
17/09/2003	**02:59**	**51.75**	**101.53**	**Mb4.6**	**55**	**136**	**23**	**8**	**25**	**267**	**196**	**74**	**114**	**318**	**29**	**35**	Radziminovich et al., 2
17/09/2003	**02:59**	**51.75**	**101.53**	**Mw4.9**	**62**	**41**	**26**	**196**	**10**	**291**	**180**	**60**	**60**	**49**	**41**	**131**	Seredkina, Melnil 2013
17/09/2003	03:31	51.76	101.58	3.7	3	328	16	59	74	228	253	50	-69	42	44	-113	Radziminovich et al., 2
20/09/2003	05:01	51.32	100.27	4.2	3	150	3	60	86	285	243	42	-86	57	48	-94	Radziminovich et al., 2
19/01/2004	**23:50**	**51.89**	**100.15**	**Mb4.5**	**48**	**342**	**37**	**130**	**16**	**233**	**4**	**44**	**152**	**115**	**71**	**50**	Melnikova et al., 2010
19/01/2004	**23:50**	**51.89**	**100.15**	**Mw4.8**	**26**	**326**	**45**	**85**	**34**	**217**	**270**	**85**	**-45**	**5**	**45**	**-173**	Seredkina, Melnil 2013
11/03/2004	09:39	52.14	100.74	Mb4.1	48	161	40	360	10	261	202	66	135	314	50	32	Melnikova et al., 2010
21/10/2004	01:00	51.7	102.25	4.1	26	356	10	261	62	152	258	72	-100	108	21	-62	Melnikova et al., 2010

11/05/2005	2:01	51.7	100.07	3.9	20	99	18	196	63	325	162	30	-128	24	67	-70	Radziminovich et al., 2
03/03/2007	11:20	51.63	99.84	3.6	44	164	10	264	44	4	264	90	100	174	10	0	Melnikova et al., 2013
03/03/2007	13:11	51.81	100.54	Mb3.6	0	154	53	64	37	244	282	65	-28	25	65	-152	Melnikova et al., 2013
05/04/2008	18:56	50.33	100.25	Mb4.5	65	142	24	336	5	244	175	55	120	310	45	55	Melnikova et al., 2014
14/05/2012	16:38	51.25	99.64	Mb4.0	63	154	1	246	27	337	71	18	95	246	72	88	Melnikova et al., 2018
16/07/2012	17:00	51.58	101.94	3.6	1	140	23	50	67	231	251	49	-59	29	50	-120	Melnikova et al., 2018
05/12/2014	**18:04**	**51.37**	**100.63**	**Mw5.0**	**3**	**293**	**70**	**33**	**20**	**202**	**245**	**79**	**-17**	**339**	**74**	**-168**	GCMT
05/12/2014	**18:04**	**51.37**	**100.63**	**5.0**	**36**	**113**	**54**	**301**	**4**	**206**	**154**	**69**	**150**	**256**	**62**	**24**	Melnikova et al., 2020
05/12/2014	**18:04**	**51.37**	**100.63**	**5.0**	**41**	**125**	**0**	**35**	**49**	**305**	**35**	**86**	**-90**	**214**	**4**	**-91**	Dobrynina et al., 2018
29/03/2019	23:22	51.65	101.57	Mw4.8	4	298	31	206	59	34	56	49	-48	182	56	-128	GCMT
11/01/2021	21:33	51.281	100.438	6.74	14	301	10	33	72	158	16	32	-110	219	60	-78	USGS
11/01/2021	21:33	51.31	100.39	6.8	13	300	33	39	54	192	354	45	-143	236	65	-52	GCMT
11/01/2021	21:33	51.21	100.47	6.7	2	295	22	26	68	199	4	47	-121	226	51	-60	GFZ
11/01/2021	21:33	51.241	100.443	6.84	9	301	33	37	55	197	358	46	-139	237	62	-52	IPGP
11/01/2021	21:33	51.32	100.42	Mb6.5	0	309	9	39	81	219	29	46	-103	228	46	0	GSRAS
11/01/2021	21:33	100.33	51.34	6.75	6	287	42	22	47	191	340	54	-146	-	-	-	This study
31/03/2021	00:01	100.29	51.35	5.1	2	130	83	239	5	39	175	84	-177	84	87	-5	GFZ

USGS, U.S. Geological Survey (https://earthquake.usgs.gov); GCMT, Global Centroid-Moment Tensor Project (https://www.globalcmt.org/); GFZ, GeoForschungsZentrum (GEOFON) Moment Tensor Solutions (http://geofon.gfz-potsdam.de/eqinfo/); IPGP, Institute de Physique du Globe de Paris (http://www.ipgp.fr/fr); GSRAS, Geophysical Survey of Russian Academy of Sciences (http://www.ceme.gsras.ru/new/ssd_news.htm).

Table S2. Details of the coseismic Sentinel-1 SAR data used in this study.

Interferograms	Primary (yyyymmdd)	Secondary (yyyymmdd)	Path	Frame	Direction	Bperp (m)
CoDT77	20201223	20210112	77	419	Descending	4.6

Note: CoDT77 is descending coseismic interferogram.

Table S3. Searching intervals of the co-seismic fault geometry parameters and the optimal solution in the non-linear inversion. E-shift and N-shift are differential E-W and N-S distances with respect to the GCMT epicenter location. Depth is the upper depth of uniform fault. The optimal solutions are maximum-a-posteriori probability solutions, and 2.5% and 97.5% represent confidence interval of posterior probability density functions of fault parameters.

Parameters	E-shift (km)	N-shift (km)	Length (km)	Width (km)	Depth	Strike (°)	Dip (°)	Rake (°)	Slip (m)
Lower boundary	-20	-20	0	0	0	0	0	-180	0
Upper boundary	20	20	40	20	15	360	90	180	5
Optimal	-8.2	2.0	35.3	14.2	3.2	340.4	53.9	-146.4	0.7
2.5%	-8.8	0.0	31.6	10.5	2.9	338.8	49.9	-152.2	0.6
97.5%	-7.5	3.0	38.1	15.6	3.8	341.4	60.9	-141.8	0.9

80 **Table S4**. Geometry information of receiver faults. Unit of ΔCFS is MPa

Faults	Strike* (°)	Dip (°)	Rake (°)	Slip-Type	Max. ΔCFS	Min. ΔCFS
NHF	341	54	-146	Dextral-Normal	2.4435	-2.5369
SHF	10	54	-146	Dextral-Normal	0.4683	-0.1780
TF	84	60	-60	Normal	0.0026	-0.0023
MF	100	75	0	Sinistral	0.1631	-0.0382
YF	289	90	0	Sinistral	0.0646	-0.0076
NDF	152	50	-80	Normal	0.0030	-0.1257
SDF	221	50	-80	Normal	0.0113	-0.0068
EGVF	0	50	110	Thrust	0.0001	-0.0001
MuF	80	90	0	Sinistral	0.0015	-0.0023

81 *Strike angle is the average striking orientation azimuth for individual receiver fault.

82

83

Reference

Delouis, B., J. Deverchere, V. Melnikova, N. Radziminovitch, L. Loncke, C. Larroque, J. F. Ritz, and V. San`kov, 2002. A reappraisal of the 1950 (Mw 6.9) Mondy earthquake, Siberia, and its relationship to the strain pattern at the south-western end of the Baikal rift zone. Terra Nova 14, 491–500.

Khilko, S. D., R. A. Kurushin, V. M. Kochetkov, L. A. Misharina, V. I. Melnikova, N. A. Gileva, S. V. Lastochkin, I. Baljinnyam, and D. Monkhoo Earthquakes and foundations of seismic zoning in Mongolia. Nauka, Moscow, 1985, 224 pp.

Golenetskii S.I. Focal mechanisms of earthquakes of Pribaikalye. In:Earthquakes in USSSR in 1976, Moscow, Nauka, 1980, p.225.

Golenetskii S.I. Focal mechanisms of earthquakes of Pribaikalye. In:Earthquakes in USSSR in 1982, Moscow, Nauka, 1986.

Filina A.G. Focal mechanisms of earthquakes of Altai-Sayan. In:Earthquakes in USSSR in 1989, Moscow, Nauka, 1993, p.375.

Solonenko, A. V., N. V. Solonenko, V. I. Melnikova, B. M. Kozmin, O. A. Kuchai, and S. S. Sukhanova. Strains and displacements in earthquake foci of Siberia and Mongolia, in Seismicity and seismic zoning of northern Eurasia 1, Moscow, 1993, 113–122.

Melnikova, V. I., Radziminovich N. A., 1998. Focal mechanisms of the earthquakes of the Baikal region for 1991–1996. Russian Geology and Geophysics 39, 11, 1598–1607.

Melnikova, V. I., Radziminovich N. A. Catalogue of earthquake focal mechanisms for the Baikal region for 1997. In: Earthquakes of the Northern Eurasia in 1997. Obninsk, GS RAS RAS, 2003, on CD.

Radziminovich N. A., Melnikova V. I., Tatomir N.V., Dobrynina A.A. Catalogue of earthquake focal mechanisms for the Baikal region for 2003. In: Earthquakes of the Northern Eurasia in 2003. Obninsk, GS RAS, 2009, on CD.

Seredkina, A., Melnikova, V., 2013. The seismic moment tensor of earthquakes in the Pribaikalye Region based on surface waves, Doklady Earth Sciences, 451 746–749 https://doi.org/10.1134/S1028334X13070064.

Melnikova, V. I., Radziminovich N. A., Tatomir N.V., Dobrynina A.A. Catalogue of earthquake

focal mechanisms for the Baikal region for 2004. In: Earthquakes of the Northern Eurasia in 2004. Obninsk, GS RAS, 2010, on CD.

Radziminovich N. A., Melnikova V. I., Tatomir N.V., Dobrynina A.A. Catalogue of earthquake focal mechanisms for the Baikal region for 2005. In: Earthquakes of the Northern Eurasia in 2005. Obninsk, GS RAS, 2011, on CD.

Melnikova, V. I., Gileva N. A., Lander A.V., Tatomir N.V. Catalogue of earthquake focal mechanisms for the Baikal region for 2007. In: Earthquakes of the Northern Eurasia in 2007. Obninsk, GS RAS, 2013, on CD.

Melnikova, V. I., Gileva N. A., Lander A.V., Seredkina A.I., Tatomir N.V. Catalogue of earthquake focal mechanisms for the Baikal region for 2008. In: Earthquakes of the Northern Eurasia, 2008. Obninsk, GS RAS, 2014, on CD.

Melnikova, V. I., Gileva N. A., Lander A.V., Seredkina A.I. Catalogue of earthquake focal mechanisms for the Baikal region for 2012. In: Earthquakes of the Northern Eurasia, 2012. Issue of 21 (2012), Obninsk, GS RAS, 2018, on CD.

Melnikova, V. I., Gileva N. A., Seredkina A.I. Catalogue of earthquake focal mechanisms for the Baikal region for 2014. In: Earthquakes of the Northern Eurasia, 2020. Issue of 23 (2014), Obninsk, GS RAS, 2020.

Dobrynina, A.A., Sankov, V.A., Tcydypova, L.R., German, V.I., Chechelnitsky, V.V., Ulzibat, M., 2018. Hovsgol earthquake 5 December 2014, Mw = 4.9: seismic and acoustic effects. Journal of Seismology, 22, 377-389.